

## **Influence of aspect ratio and pre-compression on force capacity of unreinforced masonry walls in out-of-plane two-way bending**

Chang, Lang-Zi ; Rots, Jan G.; Esposito, Rita

**DOI**

[10.1016/j.engstruct.2021.113350](https://doi.org/10.1016/j.engstruct.2021.113350)

**Publication date**

2021

**Document Version**

Final published version

**Published in**

Engineering Structures

**Citation (APA)**

Chang, L.-Z., Rots, J. G., & Esposito, R. (2021). Influence of aspect ratio and pre-compression on force capacity of unreinforced masonry walls in out-of-plane two-way bending. *Engineering Structures*, 249, 1-21. Article 113350. <https://doi.org/10.1016/j.engstruct.2021.113350>

**Important note**

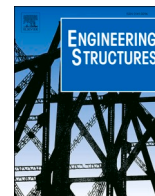
To cite this publication, please use the final published version (if applicable). Please check the document version above.

**Copyright**

Other than for strictly personal use, it is not permitted to download, forward or distribute the text or part of it, without the consent of the author(s) and/or copyright holder(s), unless the work is under an open content license such as Creative Commons.

**Takedown policy**

Please contact us and provide details if you believe this document breaches copyrights. We will remove access to the work immediately and investigate your claim.



# Influence of aspect ratio and pre-compression on force capacity of unreinforced masonry walls in out-of-plane two-way bending

Lang-Zi Chang (常浪子)\*, Jan G. Rots, Rita Esposito

Faculty of Civil Engineering and Geosciences, Delft University of Technology, Stevinweg 1, 2628 CN Delft, the Netherlands

## ARTICLE INFO

### Keywords:

Unreinforced masonry  
Out-of-plane  
Two-way bending  
Aspect ratio  
Pre-compression  
3D brick-to-brick modelling  
Analytical formulation

## ABSTRACT

Out-of-plane (OOP) failure of unreinforced masonry (URM) walls in two-way bending was widely observed after natural hazards such as earthquakes. Of various crucial factors influencing the force capacity of URM walls in OOP two-way bending (force capacity being defined as the wall peak force in terms of pressure), the pre-compression and aspect ratio (defined as the wall height to length with the height kept constant) have not been sufficiently studied. To better understand their influence, an extensive numerical study was conducted by employing a detailed 3D brick-to-brick modelling method. First, a set of monotonic quasi-static tests on full-scale walls was taken as references for calibration and validation. The numerical results matched well with the experimental results in terms of initial stiffness, force capacity and crack pattern. Afterwards, the validated model was adopted to carry out a parametric study. Results show that the force capacity of the URM walls in OOP two-way bending is exponentially related to the aspect ratio and linearly related to the pre-compression. Besides, the influence of the pre-compression and aspect ratio on the force capacity can be interdependent. Additionally, when the pre-compression is relatively low, a wall does not crack in a localized manner into several rigid plane plates at the force capacity. Instead, the deformed shape of the wall approximates a curved surface, indicating distributed rather than localized cracking at force capacity. Furthermore, the force capacity is much higher than the residual force when the rigid-plates crack pattern is formed in the post-peak stage. The parametric study also shows that torsional failure of bed joints is the predominant failure mechanism for URM walls in OOP two-way bending, and its contribution to the force capacity generally increases as the pre-compression or aspect ratio increases. Finally, the numerical results were compared with the predictions by three major analytical formulations, namely Eurocode 6, Australian Standard for Masonry Structures (AS 3700) and Willis et al. (2006). As a result, the relations between the force capacity and the aspect ratio or pre-compression derived from the numerical models could not be accurately predicted by the analytical formulations. Based on previous results, recommendations on improving the analytical formulations were proposed.

## 1. Introduction

Investigations on unreinforced masonry (URM) walls subjected to natural hazards, such as earthquakes, identify the out-of-plane (OOP) failure as one of the most common failure mechanisms [1–4]. With regard to the OOP failure, two modes can be distinguished in URM walls: one-way (mainly vertical) bending in which lateral edges of walls are not supported; two-way bending in which at least one lateral edge of walls is supported in addition to the supports at top and bottom. Compared with walls in one-way bending, walls in two-way bending are more widely encountered in practice considering that the lateral edges of walls are usually supported by pillars or return walls. Therefore, the

failure of URM walls in OOP two-way bending can be more common. According to the investigations by Dizhur et al. [5], failure of URM cavity walls in two-way bending was responsible for 57% of all OOP wall failures during the 2010/2011 Canterbury earthquakes. However, unlike the OOP one-way bending mechanism which has been well studied both experimentally and analytically [6–9], research on the OOP two-way bending mechanism is relatively limited. Furthermore, the research on the crucial factors which can have a major influence on the force capacity (defined as the wall peak force in terms of pressure in this paper) of URM walls in OOP two-way bending, such as the aspect ratio and pre-compression, is even rarer, especially in experiments [10]. Consequently, the accuracy of the evaluation on the influence of these

\* Corresponding author.

E-mail addresses: [L.Chang-2@tudelft.nl](mailto:L.Chang-2@tudelft.nl) (L.-Z. Chang), [J.G.Rots@tudelft.nl](mailto:J.G.Rots@tudelft.nl) (J.G. Rots), [R.Esposito@tudelft.nl](mailto:R.Esposito@tudelft.nl) (R. Esposito).

<https://doi.org/10.1016/j.engstruct.2021.113350>

Received 22 February 2021; Received in revised form 24 September 2021; Accepted 10 October 2021

Available online 21 October 2021

0141-0296/© 2021 The Authors. Published by Elsevier Ltd. This is an open access article under the CC BY license (<http://creativecommons.org/licenses/by/4.0/>).

crucial factors on the force capacity of walls by the analytical formulations can be hardly validated.

Experimental campaigns have been carried out worldwide to improve the understanding of the OOP two-way bending mechanism, but the total database is limited in numbers. These experiments include monotonic pushover tests [11–15], quasi-static cyclic tests [16–19] and shake-table tests [20,21]. Although these experiments successfully verified the most significant characteristics of the URM walls in OOP two-way bending such as the initial stiffness, force capacity and crack pattern, the influence of crucial factors, namely the aspect ratio (defined as the wall height to length with the former kept constant) and pre-compression, was either not specifically studied or not sufficiently studied due to a limited number of experimental samples in the experimental campaigns [10]. For example, based on 15 experimental samples with aspect ratios (height to length) of 0.67, 1 and 1.5, Ng [14] observed that the force capacity of the walls increases as the aspect ratio increases; based on 8 experimental samples subjected to pre-compression of 0, 0.05 or 0.1 MPa, Griffith and Vaculik [22] found that the force capacity of the walls increases as the pre-compression increases. These results provided general tendencies of the influence of the aspect ratio and pre-compression on the force capacity of URM walls in OOP two-way bending. However, the number of comparable samples is too limited to quantify the relations between these crucial factors and the force capacity. This brings difficulty in validating the accuracy and application range of current analytical formulations. Additionally, 4 tested walls from [22] combining aspect ratios of 0.6 and 1 and pre-compression levels of 0 and 0.1 MPa showed that as the aspect ratio changes, the increment of the force capacity caused by the pre-compression can be quite different. Although this phenomenon was observed from a limited number of experimental samples, it indicates that the influence of the aspect ratio and pre-compression on the force capacity can be interdependent, which requires a more extensive study.

As an alternative to physical experiments, finite element analysis offers the possibility of virtual experiments which is effective and cost- and time-efficient provided the models are well calibrated. Among various finite element modelling approaches, the 3D brick-to-brick modelling is one of the most promising methods to simulate at the structural components level. The 3D brick-to-brick modelling assumes that cracks and frictional slip mainly take place in mortar joints. Therefore, the mortar joints are modelled as zero-thickness interface elements, while the bricks are extended in dimensions and modelled as solid elements [23]. With this method, a balance can be found between the computational efficiency and accurate identification of the crack pattern of walls. Some studies have been conducted to predict the OOP two-way bending mechanism using the 3D brick-to-brick modelling [24–26]. Results show that major characteristics, such as stepped diagonal cracks of walls could be well captured. However, according to the authors' knowledge, this modelling method has not been applied in an attempt to quantify the relations between the aspect ratio/pre-compression and the force capacity of URM walls in OOP two-way bending.

Even though experimental and numerical samples are limited in number to compose an abundant database for various wall geometries and pre-compression levels, various analytical formulations have been proposed to evaluate the force capacity of URM walls in OOP two-way bending. Most analytical formulations are based on the following two methods or their variations: the Yield Line method proposed by Haseltine et al [27] and the Virtual Work method proposed by Lawrence and Marshall [28]. The two methods share the following similar assumptions: i) when reaching the force capacity, a wall cracks into several plane plates, ii) the crack pattern is pre-assumed, and diagonal cracks start right from wall corners, iii) the force capacity is evaluated by the principle of energy conservation, namely, moment resistance contributions along the predefined cracks are equal to the bending moment caused by OOP loads. Some fundamental differences between the two methods are i) the calculation of the moment resistance capacity along

cracks, ii) the Yield Line method assumes that all cracks develop simultaneously and the moment resistance along all cracks contributes to the force capacity; in contrast, the Virtual Work method assumes that horizontal cracks at the centre of the wall develop quite early, thus their contribution to the force capacity can be omitted, iii) the Yield Line method evaluates the slope of the diagonal cracks as an independent variable, while the Virtual Work method determines this slope based on the dimension of bricks. The correctness of these assumptions is still debatable in academia. For example, Vaculik [29] argued that the Yield Line method can be unconservative due to the assumption that cracks develop simultaneously. In opposite, Padalu et al. [30] concluded that this assumption can be accurate in evaluating the force capacity based on a crackline method (a variation of the Yield Line method). This requires further evidence with regard to crack progression in the need of justifying the assumptions and evaluating the force capacity of walls. The Yield Line method was adopted by Eurocode 6 [31]. Eurocode 6 is limited to an application range provided by its Annex E for single leaf walls with a thickness of less than 250 mm. Beyond this scope, supplementary analysis is required for the users. Besides, the predictions by Eurocode 6 are in general unconservative [10]. The Virtual Work method was adopted by the Australian Standard for Masonry Structures (AS 3700) [32], of which the expressions for bending moment capacity are empirical and dimensionally inconsistent. Based on rational deductions, Willis et al. [33] proposed new formulas for the calculations of bending moment capacities. However, the torsional strength of bed joints which is crucial to the force capacity is still empirical and requires further evaluations [10,21].

Apart from the above-mentioned drawbacks, a comparison by Chang et al. [10] between the predictions by the analytical formulations and the experimental results shows that limitations also lie in the formulations on evaluating the influence of the pre-compression and aspect ratio. For example, the formulations predict that the force capacity is not sensitive to the pre-compression, which is against the experimental results. Moreover, the predictions on the influence of the aspect ratio cannot be validated due to lack of sufficient experimental or numerical results. Also, it is still unknown whether the analytical formulations can predict the potential interdependency between the influence of the aspect ratio and pre-compression as elaborated above. Overall, these call for an extensive study on the influence of the aspect ratio and pre-compression level on the force capacity of URM walls in OOP two-way bending.

Based on the discussions above, research gaps can be revealed here: i) the available experimental samples and numerical results are limited in number in the need of sufficiently evaluating the influence of the aspect ratio/pre-compression; ii) the evaluation by the analytical formulations on the influence of the aspect ratio/pre-compression on the force capacity needs to be improved. Corresponding to these research gaps, the aims of this study are built up: i) quantify the relations between the aspect ratio/pre-compression and the force capacity of walls; ii) find the improving directions for the analytical formulations in evaluating the influence of the aspect ratio/pre-compression on the force capacity. For these purposes, nonlinear finite element analyses adopting 3D brick-to-brick models (Section 2) are employed in this study. A combined cracking-shearing-crushing model is used for interface elements at bed joint and head joint locations, while a total-strain based rotating smeared cracking model is used to simulate the cracks in bricks. Considering the experimental campaign by Griffith and Vaculik [22], the model is calibrated against the results of one wall (Section 3) and validated according to those of the other seven walls (Section 4). A parametric study considering the aspect ratio and pre-compression as variables is carried out based on the validated model. The influence of the pre-compression/aspect ratio on the load-displacement curves, force capacity, crack progression, deformation profiles and joint failure mechanisms have been explored. The relations between the force capacity and the aspect ratio/pre-compression is established with nonlinear curve fitting (Section 5). Eventually, results are compared

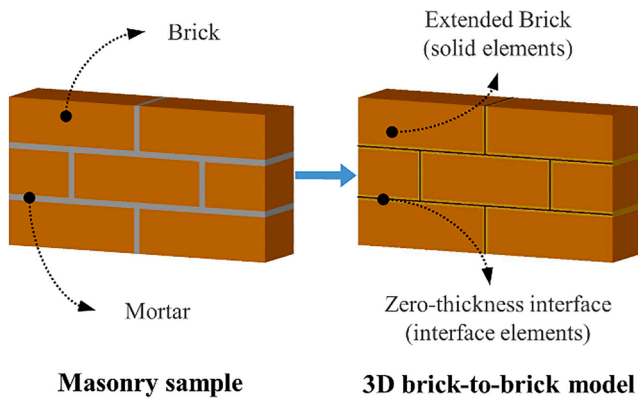


Fig. 1. Schematic diagram of 3D brick-to-brick approach.

with three analytical formulations including Eurocode 6, AS 3700 and Willis et al. (2006). Differences between the predictions by the analytical formulations and the numerical results are pointed out and explained. Suggestions regarding the improvements to the analytical formulations are proposed. (Section 6).

2. Modelling approach

Nonlinear finite element analysis, specifically, a 3D brick-to-brick modelling approach, was employed to simulate the mechanical behaviour of URM walls in OOP two-way bending in this study. With this approach, a mortar joint and its adhesive surfaces with adjacent bricks are simplified as a single zero-thickness interface and are modelled as interface elements, while the bricks are extended in dimensions (brick

height and length) and are modelled as solid elements (Fig. 1). In this case, the major geometric characteristics of walls, such as bonding pattern and tothing between the main wall and return walls, can be simulated. Therefore, the crack pattern can be explicitly identified, which is crucial for the structural response. Besides, computing efficiency can also be improved due to the simplification of the mortar joints. In this sense, this approach is suitable for modelling URM walls in out-of-plane two-way bending in this study.

A plane stress interface model formulated by Lourenco and Rots [34], namely, the combined cracking-shearing-crushing model, was applied to the zero-thickness interface elements. It is based on multi-surface plasticity, comprising a Coulomb friction model combined with a tension cut-off and an elliptical compression cap. The 3D version of this model, enhanced by Van Zijl [35], is presented in Fig. 2a. The variables of the 3D interface element are shown in Fig. 2b.

Within the elastic regime, the constitutive relations between the normal stress  $\sigma$  and the normal relative displacement  $u$ , and that between the shear stress  $\tau_s$  ( $\tau_t$ ) and the shear relative displacement  $v_s$  ( $v_t$ ), are described as follows:

$$\begin{Bmatrix} \sigma \\ \tau_s \\ \tau_t \end{Bmatrix} = \begin{bmatrix} k_{nn} & 0 & 0 \\ 0 & k_{ss} & 0 \\ 0 & 0 & k_{tt} \end{bmatrix} \begin{Bmatrix} u \\ v_s \\ v_t \end{Bmatrix} \quad (1)$$

with  $k_{nn}$  and  $k_{ss}$  ( $k_{tt}$ ) the normal and shear stiffness of the interface elements, respectively.

The tensile strength beyond the tensile strength  $f_t$  is assumed to soften exponentially (Fig. 2c):

$$\sigma = f_t e^{-\frac{f_t}{G_f^I} u} \quad (2)$$

with  $G_f^I$  the Mode-I fracture energy.

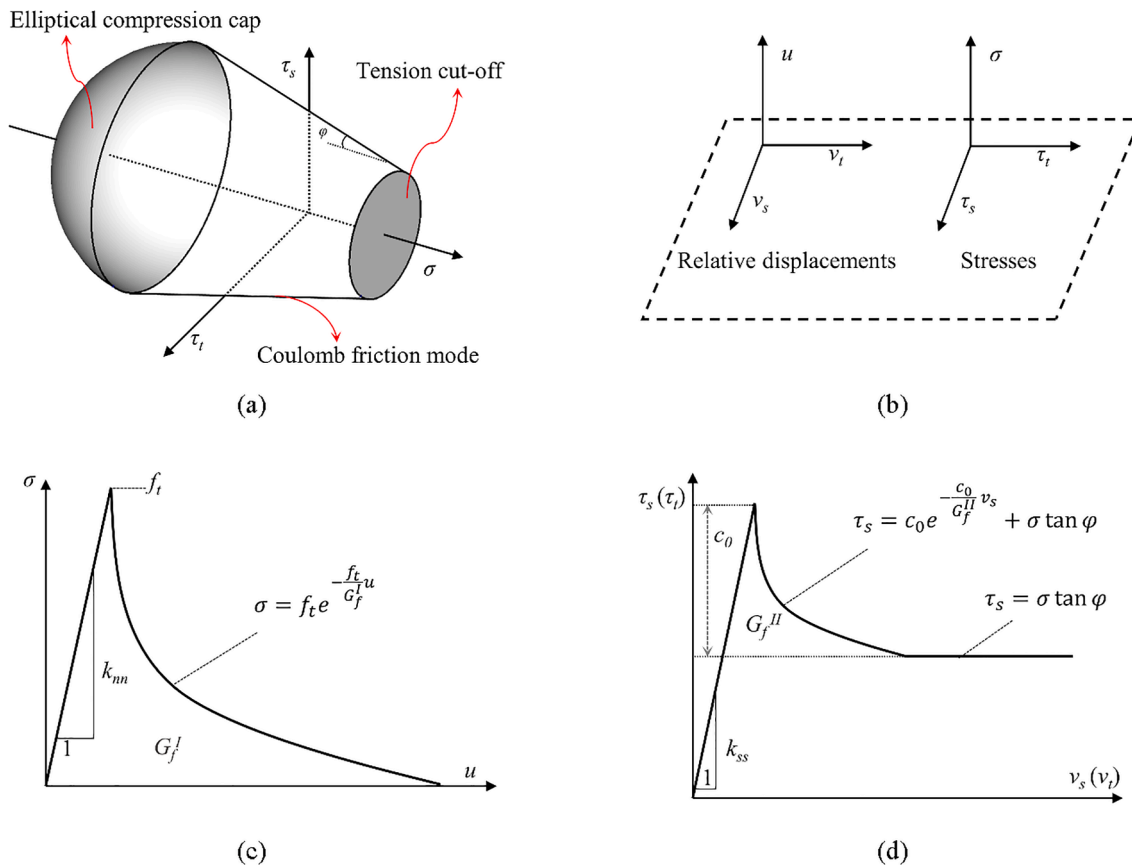


Fig. 2. Combined cracking-shearing-crushing model: (a) multi-surface plasticity model; (b) variables of the 3D interface elements; (c) tensile softening; (d) shear softening.

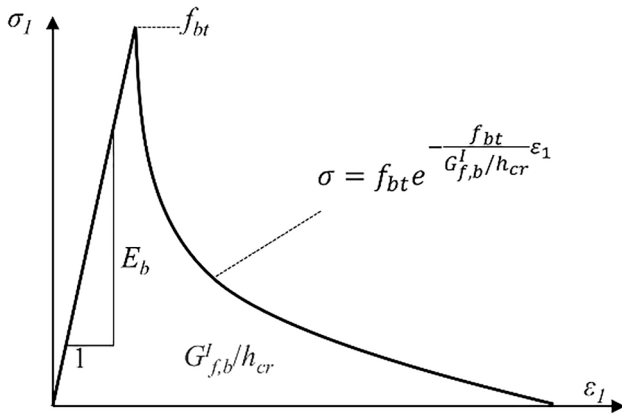


Fig. 3. Tensile softening in rotating smeared cracking model.

The Coulomb friction mode is described by:

$$\tau = \sigma \cdot \tan \varphi + c \tag{3}$$

where  $c$  is the cohesion of the brick–mortar interface and  $\varphi$  is the friction angle.

The initial cohesion of the interface softens exponentially (Fig. 2d):

$$c = c_0 e^{-\frac{\sigma_1}{G_f^{II}}} \tag{4}$$

with  $c_0$  and  $G_f^{II}$  the initial cohesion of the brick–mortar interface and

Mode-II fracture energy, respectively.

The compressive stress hardens till reaching compressive strength  $f_c$  followed by softening. Since very limited compressive failure was observed within mortar joints in the OOP two-way bending experiments, also the compressive strength of masonry is relatively high, tensile and shear failure mechanisms are thus predominant. In this sense, compressive stresses can be relatively small and remain in the elastic regime.

A rotating smeared cracking model proposed by Rots [36], namely the total strain crack model, was used to simulate potential cracks of bricks. Due to the general absence of compression failure in bricks for OOP two-way bending experiments, a linear behaviour in compression was adopted. In the tension regime, an exponential softening was adopted:

$$\sigma_1 = f_{bt} e^{-\frac{f_{bt}}{G_{f,b}^I/h_{cr}} \epsilon_1} \tag{5}$$

with  $\sigma_1$  and  $\epsilon_1$  the stress and strain along the maximum principal direction, respectively;  $f_{bt}$  the tensile strength of bricks;  $G_{f,b}^I$  the Mode-I fracture energy of the bricks, and  $h_{cr}$  the crack bandwidth (Fig. 3).

### 3. Calibration of the numerical model

#### 3.1. Experimental benchmarks

Quasi-static monotonic airbag experiments on eight walls (labelled as Wall 1–8) carried out by Griffith and Vaculik [22] were selected as benchmarks. The sketch of Wall 1 and the boundary conditions are

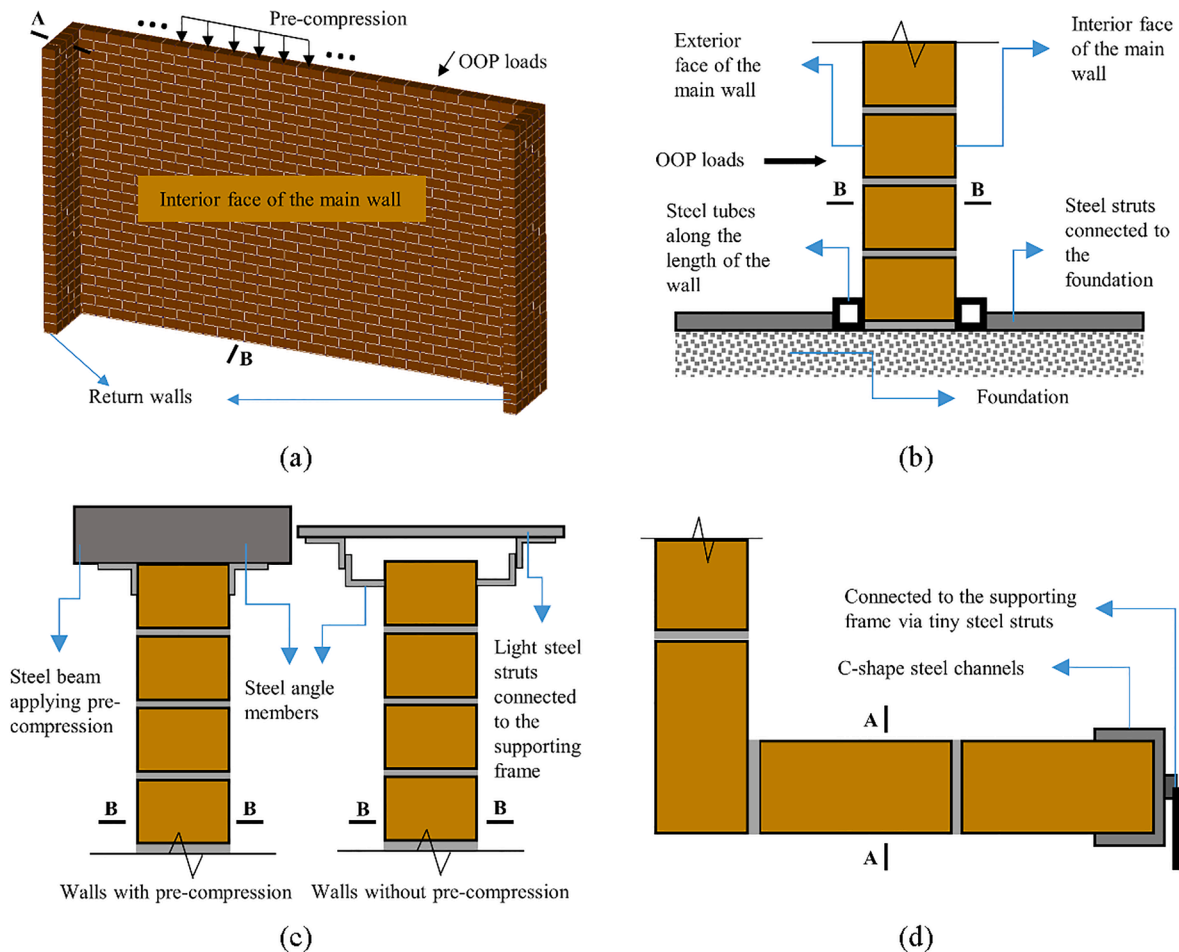
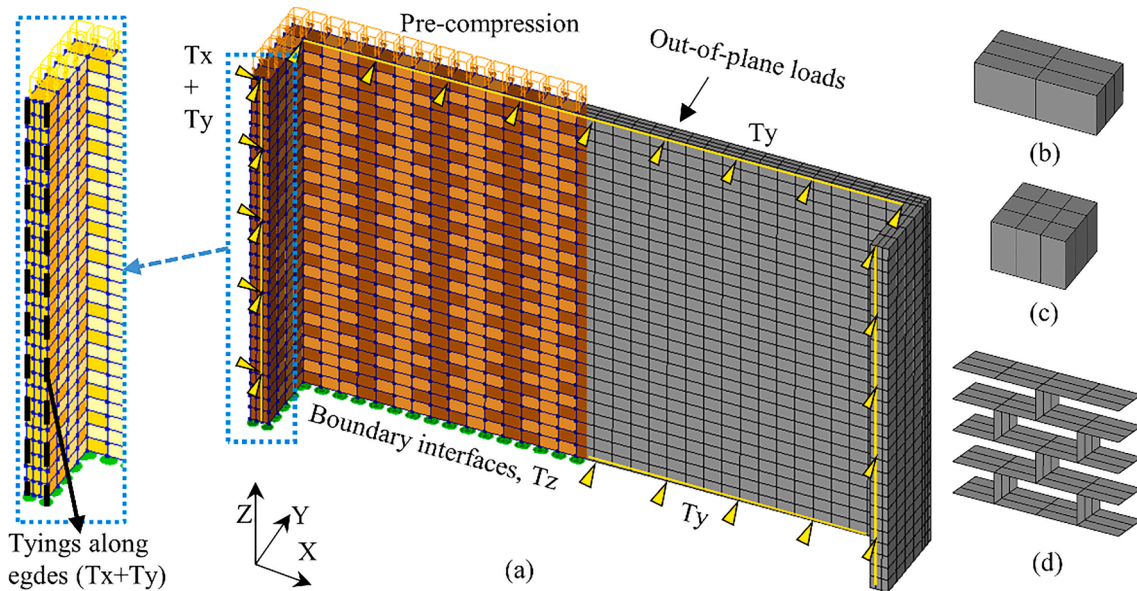


Fig. 4. Geometry and boundary conditions of the walls: (a) sketch of Wall 1; (b) boundary conditions at the bottom edge of the main wall; (c) boundary conditions at the top edge of the main wall; (d) boundary condition at the lateral edge of the return wall. (adapted from [29]).

**Table 1**  
Experimental configurations of the walls (adapted from [22]).

Experimental configurations * (dimensions in millimetres)	Wall	Pre-compression $\sigma_v$ (MPa)	Experimental configurations (dimensions in millimetres)	Wall	Pre-compression $\sigma_v$ (MPa)
	1	0.1		3	0.1
	2	0		4	0.05
	6	-		5	0
				7	0.1
				8	0

\* "S" refers to being simply supported; "R" refers to being restrained by return walls.



**Fig. 5.** Modelling settings: (a) geometry, mesh, boundary conditions and loading of the model. Tx, Ty and Tz: d.o.fs constrained in X, Y and Z directions, respectively; (b) mesh of a complete brick; (c) mesh of a half brick at intersection; (d) mesh of interface elements.

shown in Fig. 4a. In general, all walls were simply supported by steel angles and struts along the top and bottom edges of the main wall (Fig. 4b, c). One exception is Wall 6 of which the top edge was free of restraints. All walls were built with 480 mm-long return walls on lateral sides of the main wall. The lateral edges of the return walls were constrained by C-shape steel channels which were simply connected to the supporting frame (Fig. 4d). The experimental configurations of the walls are shown in groups in Table 1. These single-wythe stretcher-bonded walls were made of  $230 \times 110 \times 76 \text{ mm}^3$  clay bricks and 10 mm-thick mortar joints. All walls were 2,494 mm high. Walls 1–6 were long walls with a length of 4,080 mm, while Wall 7 and 8 were short walls with a length of 2,520 mm. Wall 1 and 2 were solid walls, while the other walls were with openings. On the top edges of Wall 1, 3 and 7, a pre-compression ( $\sigma_v$ ) of 0.1 MPa was applied, while for Wall 4 the pre-compression was 0.05 MPa. The other walls were free of pre-compression. After the application of the pre-compression, an evenly distributed OOP pressure was applied using airbags on the exterior face of the main wall. More details regarding the experimental configurations

can also be found in [29]. Here it should be noted that the displacements of the walls recorded in [29] are larger than those recorded in [22], although records in these two references were from the same experimental campaign. This is because in the former the displacements of the walls were taken as the absolute displacements at the location of interest, while the displacements of the later were corrected by reducing the rigid body movements of the supporting frames from the absolute displacements of the walls. In this sense, the corrected load-displacement relations were used as references, since rigid body movements of boundaries can be avoided in the numerical models.

### 3.2. Numerical modelling

Numerical modelling was carried out with finite element software package DIANA 10.4 [37]. Wall 1 was selected for calibration of the numerical model. Clay bricks were extended in dimensions from  $230 \times 110 \times 76 \text{ mm}^3$  to  $240 \times 110 \times 86 \text{ mm}^3$  and were modelled with 20-node quadratic solid elements. Mortar joints were modelled with zero-

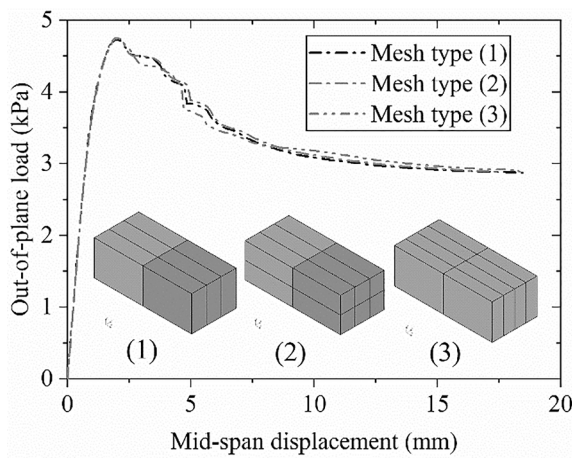


Fig. 6. Mesh sensitivity study.

Table 2  
Input parameters of bricks.

Elastic modulus $E_b$ (MPa)	Poisson's ratio $\nu_b$	Density $\rho$ (kg/m <sup>3</sup> )	Tensile strength $f_{bt}$ (MPa)	Fracture energy $G_{f,b}^I$ (N/mm)
52,700	0.16	1,900	3.55	0.00355

Table 3  
Input parameters of interface elements.

Regime	Parameter	Value
Elastic	Normal stiffness $k_{nn}$ (N/mm <sup>3</sup> )	70
	Shear stiffness $k_{ss}$ ( $k_{tt}$ ) (N/mm <sup>3</sup> )	30
	Poisson's ratio $\nu$	0.16
Tension	Tensile strength $f_t$ (MPa)	0.21
	Mode-I fracture energy $G_f^I$ (N/mm)	0.0105
Shearing	Initial cohesion $c_0$ (MPa)	0.21
	Mode-II fracture energy $G_f^{II}$ (N/mm)	0.105
	Friction angle $\varphi$ (rad)	0.523
Compression	Compressive strength $f_c$ (MPa)	16

thickness 8 + 8-node quadratic interface elements. The mesh of the model was shown in Fig. 5a. A complete brick was meshed in 2, 1 and 3 divisions in length ( $l_u$ ), height ( $h_u$ ) and thickness ( $t_u$ ) directions, respectively (Fig. 5b). At the intersections of the main wall and the return walls, half bricks were meshed in a refined manner ( $3 \times 1 \times 3$  divisions) to avoid irregular meshed shapes (Fig. 5c). The mesh manner of the interface elements follows that of the brick surfaces (Fig. 5d).

Fig. 5a shows the boundary conditions of the model. Due to the presence of tubular steel beams at the top and the bottom of the main wall on the internal face, along these edges, the wall was restrained translationally in Y direction (OOP direction). To model the mortar layer between the wall and the foundation in the experiments, the bottom face of the wall was connected to the environment using boundary interface elements which shared the same material properties as the other interface elements and were constrained along Z direction. Return walls were constrained by C-shape steel channels which were simply connected to the supporting frame. For this reason, the translation along Y direction was constrained at the central lines of the return walls. Additionally, on the left return wall at the same location, translations along X direction were constrained to prevent rigid body movements. Besides, the edges of the outer surfaces of the return walls were tied in X and Y directions so that these surfaces can keep plane when they rotate (Fig. 5a). Here it is worthy to note that it can be difficult for the numerical models to accurately capture the boundary conditions in the experiments. For example, the lateral edges of the return walls were restrained with C-shape steel channels and were connected to steel frames with only 3 tiny steel trusses. It is therefore hard to determine whether the in-plane extension of the wall should be constrained or not. Based on a sensitivity study with various boundary conditions for the return walls, it was found that if the in-plane extension of the wall was constrained, two long vertical cracks along the intersections of the main wall and the return walls would take place, which was opposite to the experimental crack patterns and signified over-restraints.

The wall was initially applied with self-weight and pre-compression in two sequential steps. Next, evenly distributed loads were applied to the exterior face of the main wall in fixed step sizes. This load was arc-length controlled with Quasi-Newton iterative method. The central point of the main wall was selected as the control point.

Fig. 6 shows the results of meshing size sensitivity study. Three mesh types have been compared: Mesh type (1) is shown in Fig. 5b; Mesh type (2) divides the bricks into  $2 \times 2 \times 3$ ; while Mesh type (3) divides the bricks into  $2 \times 1 \times 4$ . Results show that the load-displacement relations

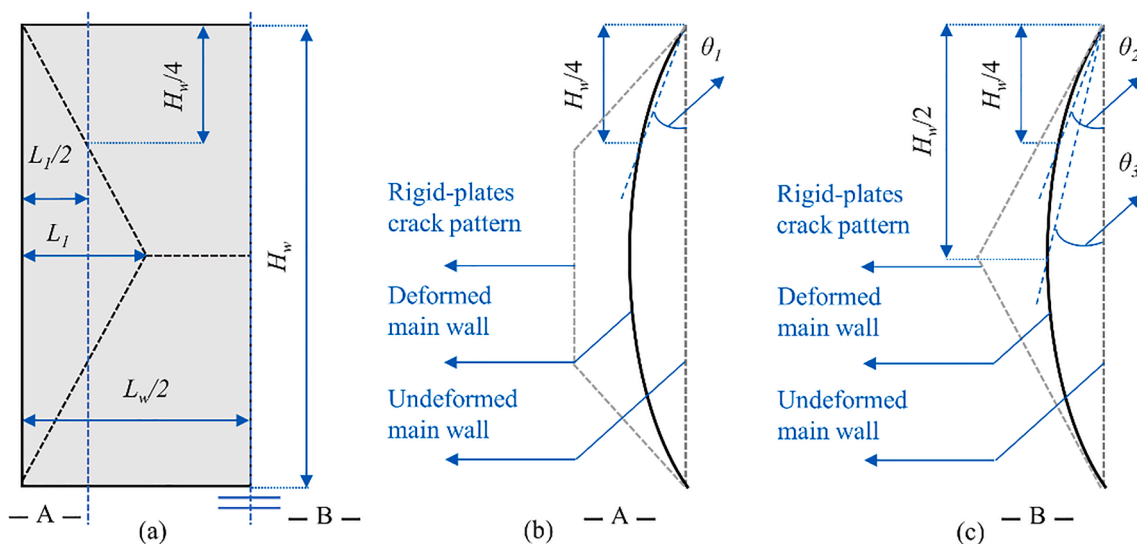
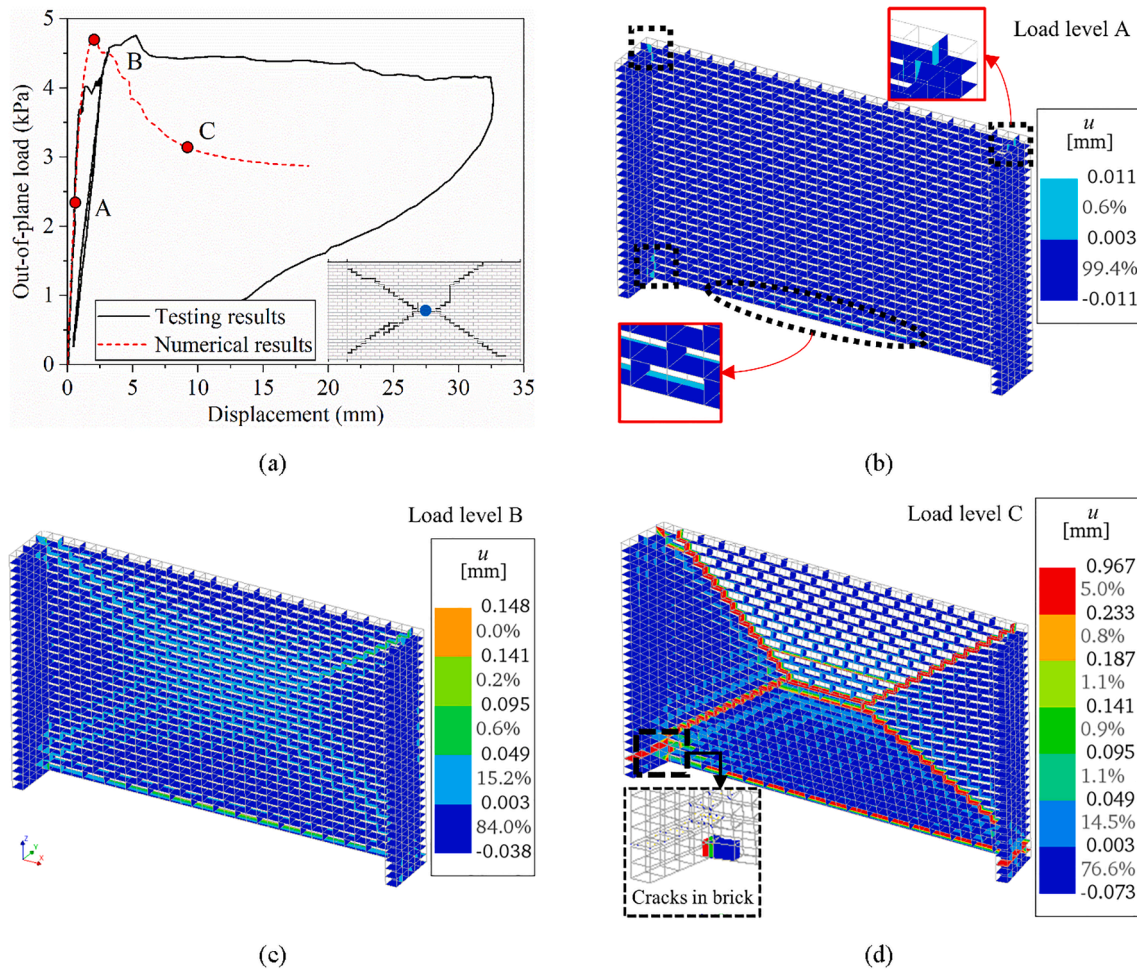


Fig. 7. Determination of instant of rigid-plates crack pattern: (a) idealised rigid-plates crack pattern shown with the left symmetric part; (b) deformed shape of the wall at section A; (c) deformed shape of the wall at section B (mid-span).



**Fig. 8.** Numerical results of Wall 1: (a) comparison with experimental results in terms of the load–displacement curve. Crack pattern from the experiment is shown at bottom right. The control point of the displacement is marked with a blue solid dot; (b)–(d) crack progression at relevant load levels (deformation scaling factor: 30,  $u$  (mm): crack opening).

**Table 4**  
Inputs for the material sensitivity study.

Variable	Model name of sensitivity study	Values of					
		$f_i$ (MPa)	$G_j^I$ (N/mm)	$\varphi$ (rad)	$c_0$ (MPa)	$G_j^{II}$ (N/mm)	Dilatancy angle $\psi$ (rad)
-	Calibrated model	0.21	0.0105	0.523	0.21	0.105	0
$f_i$	$0.75f_i$	0.1575	0.0105	0.523	0.21	0.105	0
	$1.5f_i$	0.315	0.0105	0.523	0.21	0.105	0
$G_j^I$	$0.5G_j^I$	0.21	0.00525	0.523	0.21	0.105	0
	$2G_j^I$	0.21	0.021	0.523	0.21	0.105	0
$\varphi$	$0.75\varphi$	0.21	0.0105	0.39225	0.21	0.105	0
	$1.25\varphi$	0.21	0.0105	0.65375	0.21	0.105	0
$c_0$	$0.75c_0$	0.21	0.0105	0.523	0.1575	0.105	0
	$1.5c_0$	0.21	0.0105	0.523	0.315	0.105	0
$G_j^{II}$	$0.5G_j^{II}$	0.21	0.0105	0.523	0.21	0.0525	0
	$2G_j^{II}$	0.21	0.0105	0.523	0.21	0.21	0
Dilatancy angle $\psi$	Dilatancy considered	0.21	0.0105	0.523	0.21	0.105	0.37

derived from various meshed models are very similar to each other. In this study, Mesh type (1) with the least number of elements is used for the sake of computational efficiency.

### 3.3. Calibration of material properties

In this paper, the material variability and the strength difference between bed and head joints were not considered. This aims at focusing on the influence of the pre-compression and aspect ratio in the later

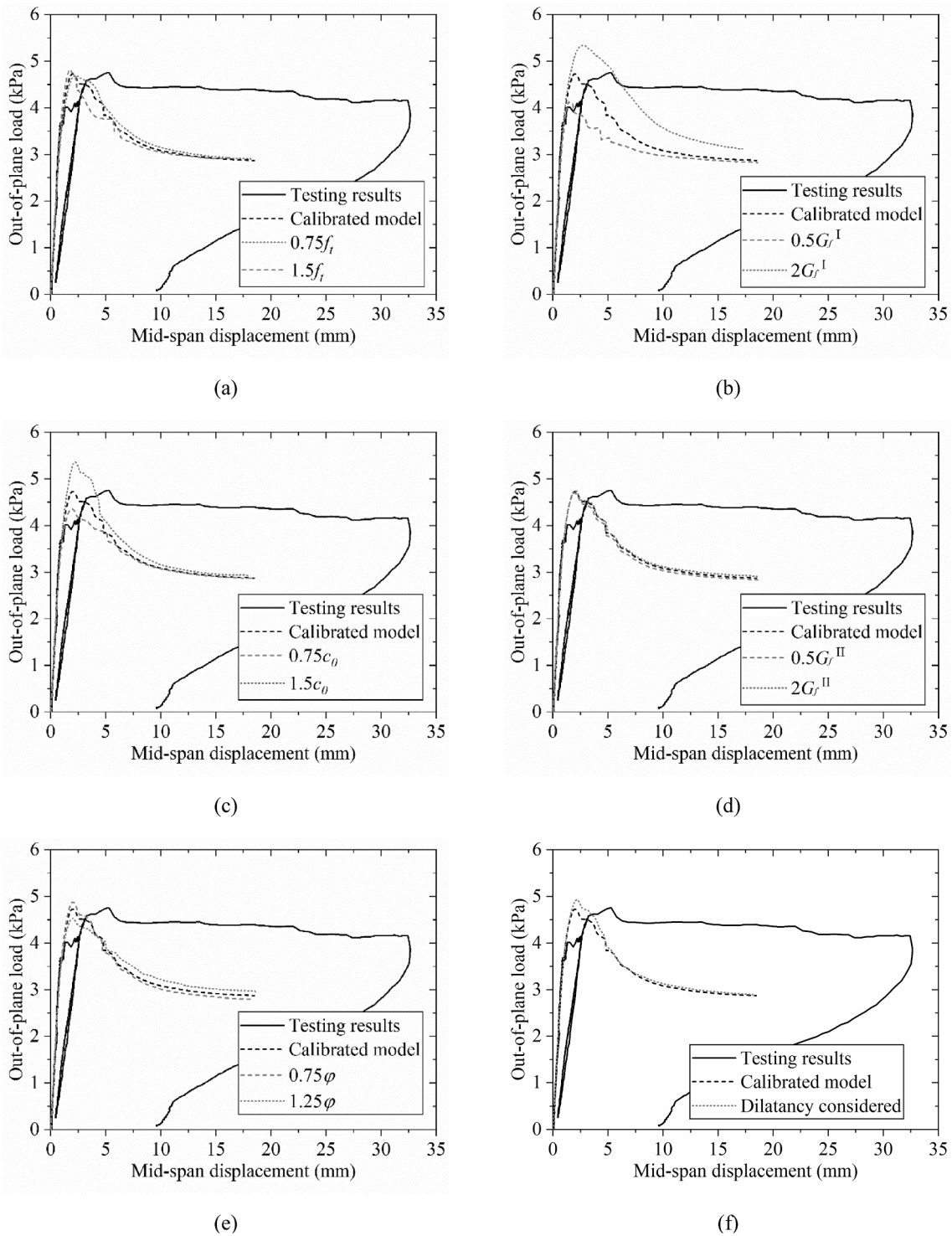


Fig. 9. Material sensitivity study (a)-(f) on: tensile strength  $f_b$ , mode-I fracture energy  $G_f^I$ , cohesion  $c_\theta$ , mode-II fracture energy  $G_f^{II}$ , friction angle  $\varphi$  and dilatancy angle  $\psi$  as single variable, respectively.

study.

For the bricks (Table 2), the elastic modulus ( $E_b$ ) and tensile strength ( $f_{bt}$ ) were derived from the material experiments in the same experimental campaign [22], while other parameters were assumed. Mode-I fracture energy of bricks ( $G_{f,b}^I$ ) was assumed to be rather small considering the brittle nature of the bricks. The Poisson's ratio ( $\nu_b$ ) is assumed as 0.16. The density of bricks was assumed to be equal to the density of the masonry ( $\rho$ ). The crack bandwidth used in the rotating smeared cracking model for the bricks was set as 10 mm. The crack bandwidth

was not calculated as the cubic root of the element volume as suggested by Rots [36]. Otherwise, the overly small value of  $G_{f,b}^I/h_{cr}$  can cause snap-back, therefore leading to numerical errors.

For the input parameters of interface elements (Table 3), limited information was available from the experiments. Therefore, calibration was carried out based on available literature. After the boundary conditions of the wall were determined as in Section 3.2, the normal stiffness ( $k_m$ ) and shear stiffness ( $k_{ss}$  and  $k_{tt}$ ) of the interface elements were calibrated by conducting a preliminary linear elastic analysis.  $k_m$  and  $k_{ss}$

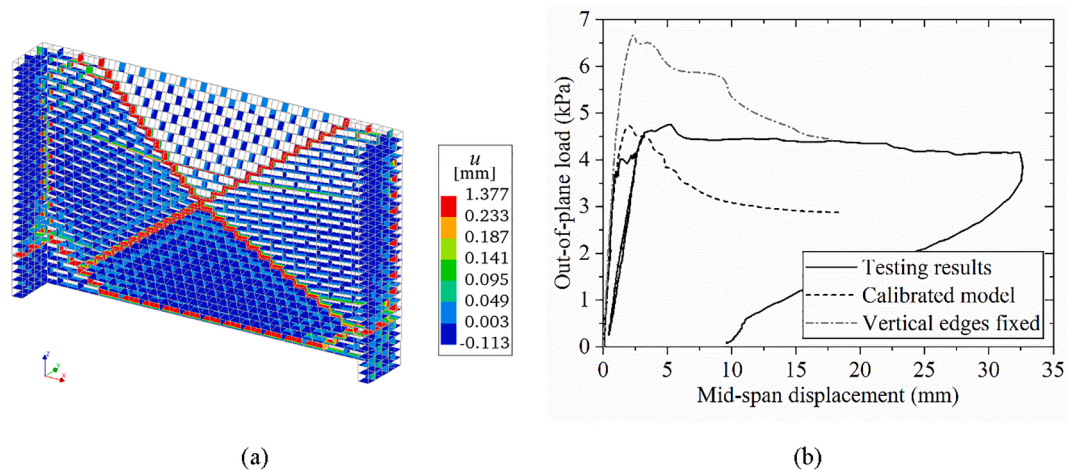


**Fig. 10.** Sensitivity study on the rotational stiffness of the boundary conditions: (a) the crack pattern of the wall with lateral edges fixed; (b) force–displacement curves of the calibrated model and the model with the vertical edges fixed.

( $k_{tt}$ ) also follow the relationship in Eq. (6). The same Poisson's ratio adopted for the brick was used for the interface elements. The criterion for the calibration of the stiffness of the interfaces is to make the initial stiffness of the model match with that of the experimental sample. The tensile strength of the interfaces ( $f_t$ ) was assumed as 1/3 of the flexural strength from bond wrench tests ( $f_{x1}$ ) as recommended in [38] and [26]. The cohesion ( $c_0$ ) was equal to  $f_t$  as recommended in [39]. Friction angle ( $\varphi$ ) was taken as that of the half-scale bricks from a similar experimental campaign in [29]. Mode-I fracture energy ( $G_f^I$ ) was taken as 0.05 times of  $f_t$  referring to [23,39,40]. Mode-II fracture energy ( $G_f^{II}$ ) was calibrated to make the force capacity of the model match with that of the experimental sample. The compressive strength ( $f_c$ ) was derived from the experiments. The dilatancy angle was set to zero, implying non-associated plasticity with zero uplift upon shearing, because Ref. [41] shows that the dilatancy is insignificant when tensile failure between bricks and mortar joints is the major failure mechanism.

$$k_{ss}(k_{tt}) = \frac{k_{nn}}{2(1+\nu)} \quad (6)$$

### 3.4. Numerical results

The results of the calibration against Wall 1 in terms of the load–displacement curve and crack progression are presented and discussed in this section. The displacement of wall 1 was determined in the centre of the wall as in the experiments. Besides, it is important to determine the instant when the wall cracks into several rigid plane plates (hereinafter, referred to as rigid-plates crack pattern). This is because all analytical formulations evaluate the force capacity at the moment when the deformed shape of the wall consists of several rigid plane plates. It is, therefore, necessary to verify this assumption with the numerical results. The instant of the rigid-plates crack pattern is determined satisfying the following two criteria at the same time: i) at the mid-span of the wall, the difference between the angle of the upper 1/2 height of the deformed wall and the undeformed wall, and that of the upper 1/4 height of the deformed wall and the undeformed wall ( $\theta_3$ , and  $\theta_2$ , respectively) should be less than 10%; ii) the difference between the angle of the upper section of the deformed wall above the central point of the diagonal crack and the undeformed wall ( $\theta_1$ ) and  $\theta_3$  should be less than 10% (Fig. 7). After slight adaptations, these criteria are also suitable for narrow walls having central vertical cracks.

The predicted initial stiffness and force capacity of the wall are in good agreement with the experimental results (Fig. 8a). Fig. 8b, c and d corresponding to 3 marked load levels A, B and C in Fig. 8a show the onset of cracking, the instant of reaching the force capacity and the

instant of rigid-plates crack pattern, respectively. In the legends of interface crack openings,  $u = 0.003$  mm and  $u = 0.233$  mm correspond to the onset of cracking and fully opened crack when the tensile stress reduces to 1/100 of the tensile strength  $f_b$ , respectively. The grey text in the legends indicates the percentage of integration points corresponding to each contour level. At load level A, when the initial stiffness of the wall starts to degrade, only 0.6% of integration points in the interface elements reach the onset of cracking at four corners and the bottom of the wall (Fig. 8b). When the force capacity of the wall is reached (load level B), 16% of the integration points surpass the tensile strength, though none of them fully crack. At the same time, diagonal and central cracks start to form. As 5% of the integration points on the interface elements fully crack, the rigid-plates crack pattern starts to form (Fig. 8d, load level C). At this stage, the model shows the typical crack pattern of long URM walls in two-way bending, i.e. diagonal cracks and central horizontal crack, which matches well with the experimental crack pattern shown in Fig. 8a. After this, the major cracks keep opening, and the deformed shape of the wall remains the same. Compressive failure of interfaces was not detected and stresses remained in the elastic regime. Besides, only a few bricks crack at the corners of the main wall (Fig. 8d). This is in agreement with the experimental evidence that cracks in bricks can be insignificant.

### 3.5. Sensitivity study on material properties and boundary conditions

Although the numerical model matches well with the experimental results in terms of the initial stiffness, force capacity and rigid-plates crack pattern, the force capacity drops more sharply than that in the experiment (Fig. 8a). This phenomenon has also been observed by Karimi Ghaleh Jough and Golhashem [42] who also used the 3D brick-to-brick modelling approach to predict the force capacity of URM walls in OOP two-way bending. In fact, according to the shake-table tests by Graziotti et al. [21] and monotonic static tests by Lawrence [43] on the URM walls in OOP two-way bending, the wall capacity decreased sharply after reaching the peak.

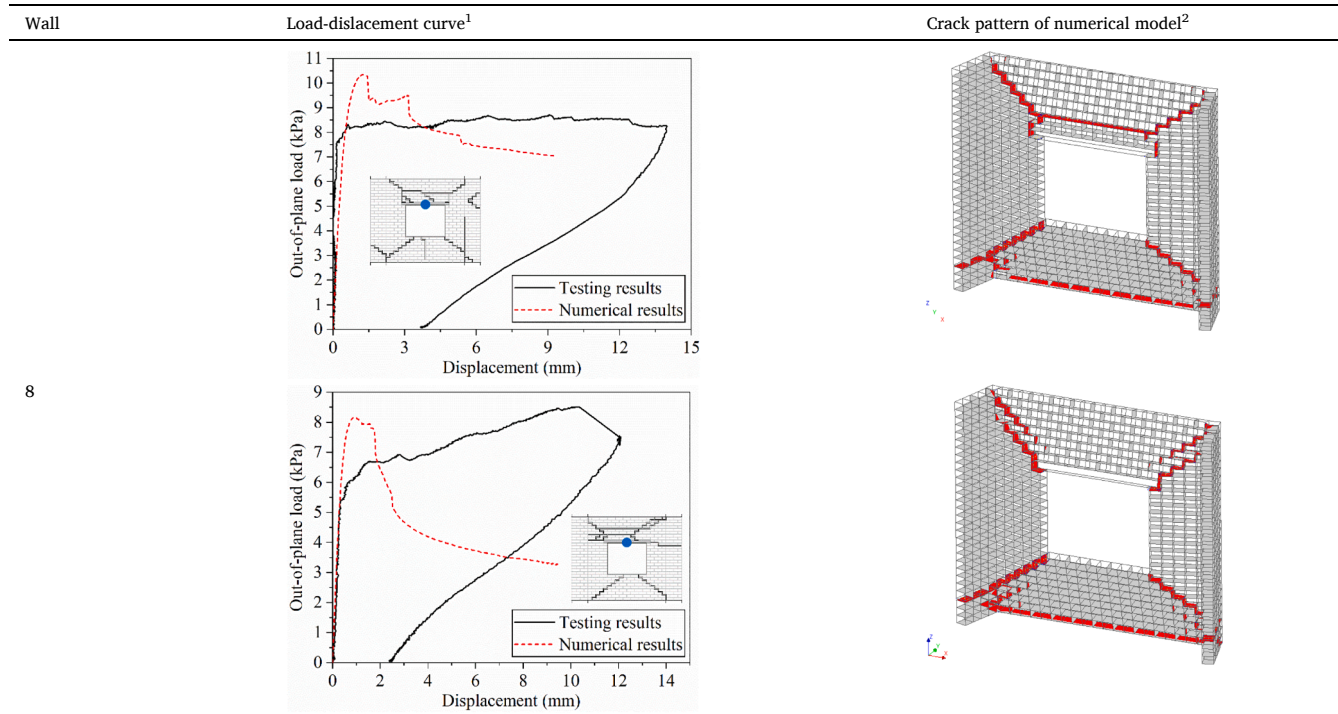
A sensitivity study was carried out to examine whether the adjustment of these parameters can reduce the difference between the numerical and experimental results. The tested models are listed in Table 4. In each model, only one variable was varied based on the calibrated model, while the other four variables were kept unchanged. At the same time,  $c_0$  should be larger than  $f_t \cdot \tan\varphi$  (satisfying Eq. (3)). The results of the sensitivity study are shown in Fig. 9. Fig. 9a, d, e and f show that within the studied ranges, the force capacity and residual force of the wall is insensitive to the tensile strength  $f_b$ , mode II fracture energy  $G_f^{II}$ , friction angle  $\varphi$  and dilatancy  $\psi$ . Fig. 9b and c show that the force

**Table 5**  
Validation of the numerical model in terms of the load–displacement curves and crack pattern.

Wall	Load-displacement curve <sup>1</sup>	Crack pattern of numerical model <sup>2</sup>
2		
3		
4		
5		
6		
7		

(continued on next page)

Table 5 (continued)



<sup>1</sup> Tested crack patterns are shown in the load–displacement graphics. Positions of recorded displacements are marked with blue dots.

<sup>2</sup> Cracks where  $f_t$  reduces to its 1/100 are marked with red. Deformation scaling factor: 20.

Table 6

Comparison in terms of initial stiffness and force capacity between the numerical and experimental results.

Wall	Experiments		Numerical results		Errors (numerical results to experiments)	
	Initial stiffness $K_{ini}$ (kPa/mm)	Force capacity $w$ (kPa)	Initial stiffness $K_{ini}$ (kPa/mm)	Force capacity $w$ (kPa)	Regarding $K_{ini}$	Regarding $w$
1	4.27	4.76	4.37	4.73	2%	-1%
2	0.72	3.04	4.36	3.68	505%	21%
3	5.38	5.05	4.60	5.32	-14%	5%
4	5.34	3.91	4.58	4.65	-14%	19%
5	4.86	3.59	4.53	4.01	-7%	12%
6	1.10	1.97	1.23	2.44	12%	24%
7	19.95	8.71	19.78	10.36	-1%	19%
8	17.37	8.52	19.74	8.17	14%	-4%
Average <sup>1</sup>	-	-	-	-	-	11%

<sup>1</sup> Wall 2 is excluded.

capacity is sensitive to the mode I fracture energy  $G_f^I$  and the initial cohesion  $c_0$ , while the residual force is not. In all numerical cases, the difference between the force capacity and the residual force is larger than that in the experiment.

Another sensitivity study has been carried out to examine whether changing the boundary conditions can improve the ductility of the wall. Different from the calibrated model, the lateral edges of the return walls are fixed in the varied case. Comparisons show that when the lateral edges of the return walls are fixed, cracks develop between the intersection of the main wall and the return walls (Fig. 10a), and the crack pattern is different from that in the experiment (Fig. 8a). Besides, changing the boundary conditions does not improve the ductility of the wall, as shown in Fig. 10b.

#### 4. Validation of the numerical model

In this section, the validation of the calibrated model is reported for

the other seven walls in the same experimental campaign. For Wall 3–8, the steel tubes used as lintels above the openings were modelled with linear elastic solid elements using material properties of steel (Elastic modulus: 210 GPa; Poisson's ratio: 0.3). Since the presence of openings caused difficulty to determine the instants of forming rigid-plates, the crack patterns at the end of analysis were compared with those from experiments for simplicity. Results are shown in Tables 5 and 6.

Comparing the numerical and experimental results, it can be seen that the numerical models predict the crack patterns to a rather accurate degree (Table 5). Specifically, the stepwise diagonal cracks are well captured. Cracks of bricks are not presented here, since they only take place at the corners of the walls, similar to Wall 1 (Fig. 8d). Compressive failure of bricks and interface elements are not detected.

A good agreement is found in terms of initial stiffness and force capacity (Table 6). Special attention should be paid to Wall 2. In the experiment, Wall 2 was not sufficiently constrained at the bottom in the out-of-plane direction, which led to large sliding after being loaded [29].

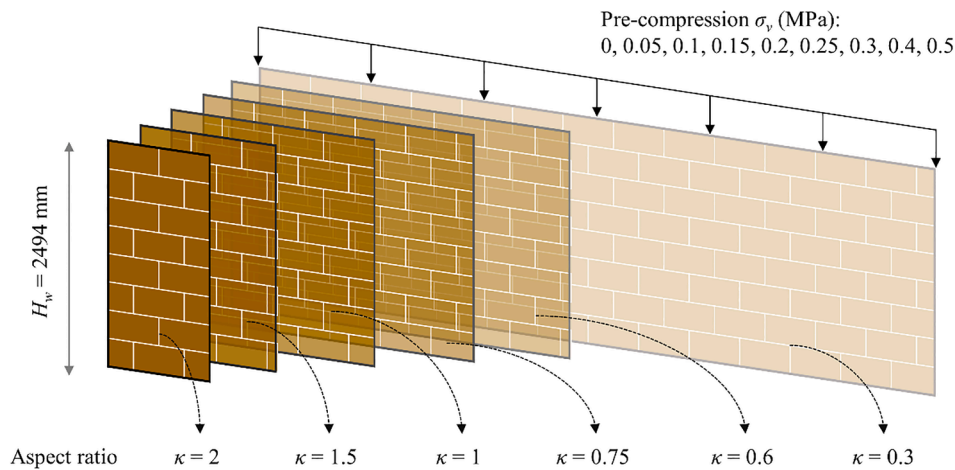


Fig. 11. Schematic diagram of wall configurations in the parametric study (return walls are not presented).

Therefore, the predicted initial stiffness  $K_{ini}$  and force capacity  $w$  of Wall 2 are higher than those of the experimental results (Table 6). Apart from this, a maximum deviation of 14% is found in terms of initial stiffness. This suggests that the boundary conditions and material properties in the elastic range are well calibrated. As for the force capacity, the numerical results match well with the experimental results, though on average it is 11% over-estimated. These differences can be attributed to not considering the spatial variability in the modelling. According to Li et al. [44], if the material properties vary randomly among different mortar joints on the same wall, the error between predictions and the tested force capacity can range from  $-25\%$  to  $30\%$ . In the present study, deterministic values of the material properties were used for all interfaces on the same wall. The predicted differences are likely to be caused by excluding the spatial variability of the material properties. Overall, the accuracy of the calibrated model was validated by applying it to the other seven walls. Therefore, the validated model can be used for further parametric study.

## 5. Parametric study

To study the influence of aspect ratio and pre-compression, a parametric study was carried out based on the validated model. Six different values of aspect ratio and nine values of pre-compression were selected for a total of 54 analysis combinations (Fig. 11). The aspect ratio  $\kappa$  (wall height to length,  $H_w/L_w$ ) ranged between 0.3 and 2 as suggested by Annex E in Eurocode 6 [31]. For each wall geometry, the values of pre-compression  $\sigma_v$  range from 0 to 0.5 MPa. The value of 0.5 MPa was estimated in the following way. Considering a typical two-storey detached or terraced house with an attic [45,46], the pre-compression from one concrete floor (spanning 6 m and 0.2 m thick) can be 0.15 MPa, the variable load on each floor can be 0.03 MPa, the self-weight from the upper masonry walls can be 0.05 MPa per storey, the load from the roof can be 0.05 MPa. The pre-compression on the top edge of the bottom wall then sums up to values close to around 0.5 MPa. Apart from the aspect ratio and pre-compression, all the other settings, e.g. input parameters of materials, return walls, bonding patterns and boundary conditions, are the same as presented in Section 3. Please note the results of the parametric study are limited to typical weak mortar/strong brick masonry which generally represents clay brick masonry.

### 5.1. Load-displacement curve and force capacity

Fig. 12 shows the load-displacement curves of all walls in the parametric study. In this figure, the force capacity is marked with blue dots; the instants of forming rigid-plates crack pattern are determined according to the criteria proposed in Section 3.4 and marked with solid

red dots; for walls that did not reach the rigid-plates crack patterns, instants of crack patterns are marked with empty red dots at the end of the analysis. A general tendency observed is that as the aspect ratio  $\kappa$  or pre-compression  $\sigma_v$  increases, the force capacity increases accordingly. The relation between the force capacity and the aspect ratio, the relation between the force capacity and the pre-compression, are graphically presented in Fig. 13a and b, respectively. Results show that the force capacity can follow an exponential relation with aspect ratio and a linear relation with pre-compression, respectively. This was confirmed by a preliminary fitting analysis selecting aspect ratio or pre-compression as the single independent variable and the force capacity as the dependent variable. Additionally, Fig. 13b shows that as the aspect ratio increases, the slopes of the curves also increase. This implies that the influence of the pre-compression and aspect ratio can be interdependent.

### 5.2. Crack progression and deformation profile

Table 7 presents the crack progression of walls with all aspect ratios subjected to pre-compression of 0.1, 0.3 and 0.5 MPa. For each wall, crack progression is shown at two stages, namely at the force capacity and final crack pattern. Concerning the latter, crack patterns of the walls corresponding to the instants marked with solid and empty red dots in Fig. 12 are presented. At the force capacity, interface crack opening  $u$  larger than 0.003 mm (onset of the crack of integration points) and smaller than 0.233 mm (integration points fully crack) is marked in blue;  $u$  larger than 0.233 mm is marked in red. At final crack pattern,  $u$  is only marked in red when it is larger than 0.233 mm. Table 7 shows that when the walls reach the force capacity, multiple diagonal and central cracks develop simultaneously. Furthermore, at this stage integration points on interface elements hardly fully crack unless the pre-compression is over 0.3 MPa. At final crack pattern, the pre-compression has very limited influence on the deformed shapes of the walls, while the crack patterns change obviously as the aspect ratio increases, i.e., central horizontal crack transforms into a central vertical crack. The tensile failure of the bricks of various cases is shown in Fig. 14. The results show that the failure of the bricks is primarily taking place at the corners of the wall and has almost no effect on the overall behaviour regardless of the pre-compression and aspect ratio.

The deformation profiles of four representative walls at different instants are shown in Fig. 15. Results show that when the pre-compression is low (0.1 MPa), the deformation profiles of the walls at the force capacity approximates curved surfaces, while those at the rigid-plates crack pattern are identical to each other and are close to bi-linear lines (Fig. 15a,c). When the pre-compression is high (0.5 MPa), the rigid-plates crack pattern does not form at the end of the analysis, although the deformation profiles are close to bi-linear lines (Fig. 15b,

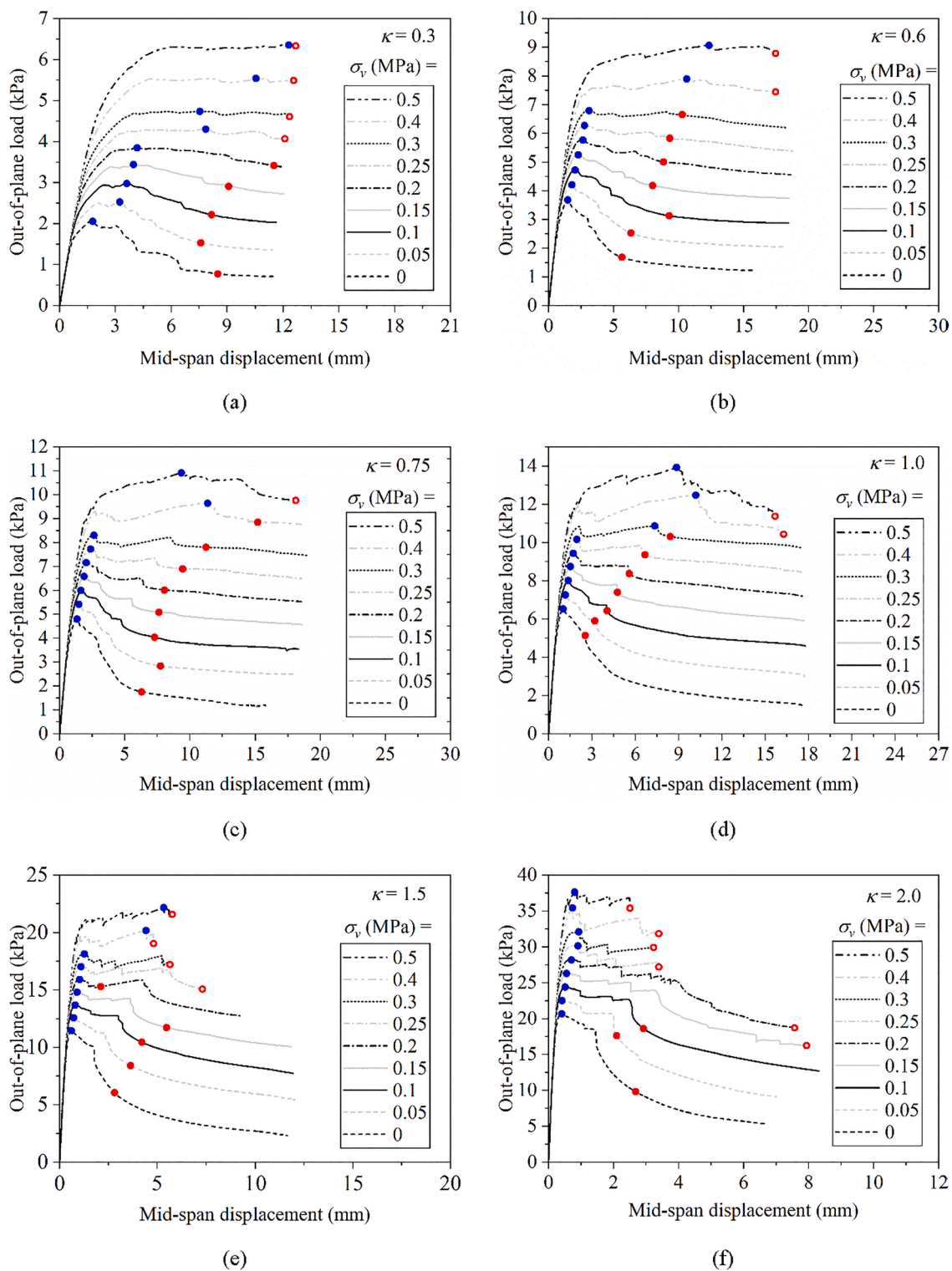


Fig. 12. Load-displacement curves obtained from the parametric study regarding aspect ratio  $\kappa$  and pre-compression  $\sigma_v$ : (a)  $\kappa = 0.3$ ; (b)  $\kappa = 0.6$ ; (c)  $\kappa = 0.75$ ; (d)  $\kappa = 1.0$ ; (e)  $\kappa = 1.5$ ; (f)  $\kappa = 2.0$ . Force capacity  $w$  is marked with blue dots. Instants of forming rigid-plates crack pattern are marked with solid red dots. For walls that did not reach the rigid-plates crack patterns, instants of crack patterns are marked with empty red dots at the end of the analysis.

d). Furthermore, the differences between the force capacity  $w$  and the force at rigid-plates crack pattern  $w_{cp}$  of the walls can be large especially when the pre-compression is relatively small, as shown in Fig. 16. This is because on one hand, the increase of the pre-compression increases the arching effect. On the other hand, the increase of the pre-compression increases the friction and shear fracture energy between the

interfaces. Therefore, the wall needs to dissipate more energy to reach the force capacity. These effects together increase the ductility of the wall. In contrast, current analytical formulations assume that the force capacity is reached at the rigid-plates crack pattern. The above-mentioned observations from numerical results, however, indicate that this assumption can lead to large inaccuracy in evaluating the force

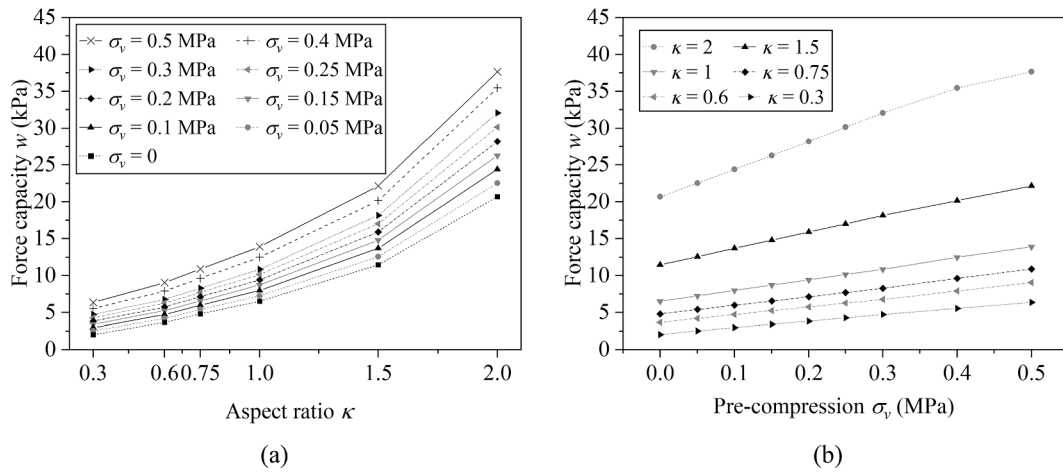


Fig. 13. Force capacity  $w$  in relations with (a) aspect ratio  $\kappa$  and (b) pre-compression  $\sigma_v$ .

capacity especially for walls under low pre-compression. Therefore, the deformation shape at the force capacity is suggested to be re-evaluated to improve the accuracy of the analytical formulations.

### 5.3. Joint failure mechanisms

Under OOP two-way bending, generally the crack pattern of the URM walls is “X” shaped (Fig. 17a). Besides, four kinds of joint failure mechanisms, namely bending and torsional failure of bed and head joints, majorly contribute to the force capacity of walls (Fig. 17b) [33]. Considering this, it is important to determine how the pre-compression or aspect ratio influence the performance of these failure mechanisms therefore influencing the force capacity. With this purpose, the following procedure was built for the comparison of the dissipated energy among different walls: i) major cracks, in which diagonal and horizontal/vertical cracks can be easily distinguished, were determined based on the final crack patterns as shown in Fig. 17a and Table 7; ii) along the major cracks, crack failure was categorised into five kinds: bending and torsional failure of bed and head joints at diagonal cracks, and bending failure of bed joints at central horizontal cracks or bending failure of head joints at central vertical cracks; iii) dissipated mode-I and mode-II fracture energy of interface elements were selected as indicators of the bending and torsional behaviour of joints, respectively; iv) dissipated mode-I and mode-II fracture energy of a single joint were calculated separately from the start of loading to the moment of reaching the force capacity; v) dissipated energy of counted joints on the major cracks was summed according to crack failure categories; vi) contributions of dissipated energy of different joint mechanisms were compared.

On one single joint, the total dissipated mode-I and mode-II fracture energy due to bending and torsion, respectively, were calculated using the following equations:

$$E_{GII} = \left( \sum_{j=1}^n \sum_{i=1}^t \sigma_{j,i} \cdot (u_{j,i} - u_{j,i-1}) \right) \cdot \frac{A_{joint}}{n} \quad (7)$$

$$E_{GIII} = \left( \sum_{j=1}^n \sum_{i=1}^t \tau_{j,i} \cdot (v_{j,i} - v_{j,i-1}) \right) \cdot \frac{A_{joint}}{n} \quad (8)$$

where  $E_{GII}$  and  $E_{GIII}$  are total fracture energy dissipated by bending and torsion in a single joint, respectively;  $t$  is the step when the wall reaches the force capacity;  $n$  is the number of integration points on one joint;  $\sigma$  and  $\tau$  are normal and shear stress, respectively;  $u$  and  $v$  are normal and shear relative displacement, respectively;  $A_{joint}$  is the area of a joint.

To study the influence of the pre-compression on the performance of the joint failure mechanisms, walls of aspect ratio 0.6 were compared. The positions of the major cracks are the same for all walls. Results in

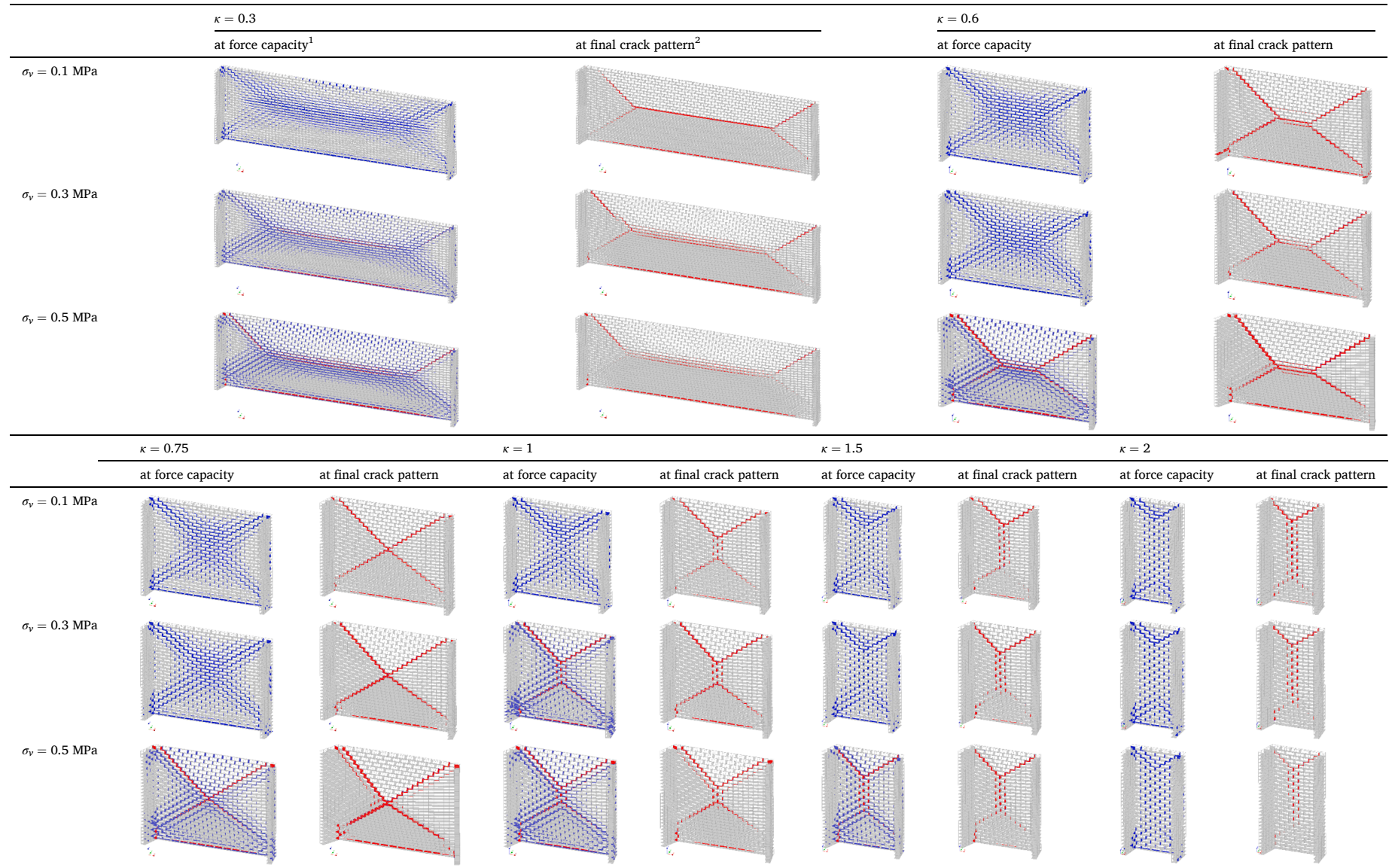
Fig. 18a show that generally the fracture energy dissipated by all joint failure mechanisms increases as the pre-compression increases. This suggests that all failure mechanisms contribute to the increase of the force capacity as the pre-compression increases. When the pre-compression is above 0.3 MPa, the dissipated fracture energy increases sharply. This is because the walls subjected to high pre-compression reach their force capacity quite late, and the cracks develop more completely thus leading to a high dissipation of fracture energy. Proportions of contributions by different joint failure mechanisms at different levels of pre-compression are shown in Fig. 18b. Results show that the contribution by the torsional failure of bed joints at diagonal cracks is predominant and increase as the pre-compression increases. The contributions by the torsional failure of head joints and bending failure of bed joints at diagonal cracks are close to each other and decrease as the pre-compression increases. The contribution of the bending failure of head joints at diagonal cracks are relatively small and decrease when the pre-compression is over 0.3 MPa. The contributions of the bending failure of bed joints at the central horizontal cracks are nearly negligible.

To study the influence of the aspect ratio on the performance of the joint failure mechanisms, walls subjected to 0.1 MPa pre-compression were compared. The total dissipated fracture energy of each wall was divided by the wall area. Results in Fig. 19a show that the dissipated fracture energy per unit area is following an exponential relation with the aspect ratio, which is similar to that between the force capacity and the aspect ratio (Fig. 13a). In Fig. 19b, contributions of the joint failure mechanisms show that when the aspect ratio is very low (0.3), the bending failure of bed joints at central horizontal cracks are predominant. Actually, when the wall aspect ratio is low, the wall behaviour is more close to one-way bending (Table 7). Apart from this case, the torsional failure of bed joints at diagonal cracks is predominant for other cases. Besides, the torsional failure of head joints at diagonal cracks is also important. In general, the sum contributions of the torsional failure of bed and head joints increases as the aspect ratio increases. In contrast, the contributions by the bending failure at diagonal cracks decrease as the aspect ratio increases.

### 5.4. Quantification of the influence of the pre-compression and aspect ratio

In an attempt to quantify the influence of the aspect ratio and pre-compression on the force capacity, a function of two variables based on the numerical results was nonlinearly fitted selecting the force capacity as the dependent variable and the aspect ratio and pre-compression as double independent variables. In Eq. (9),  $w_{fitted}$  is the fitted force capacity, while  $a_1$ - $a_5$  are constants. Fig. 20 shows that the

**Table 7**  
Crack progression of walls (deformation scaling factor: 30).



<sup>1</sup> Crack openings ( $w$ ) larger than 0.003 mm and smaller than 0.233 mm are marked in blue; crack openings larger than 0.233 mm are marked in red.

<sup>2</sup> Only crack openings larger than 0.233 mm are marked in red.

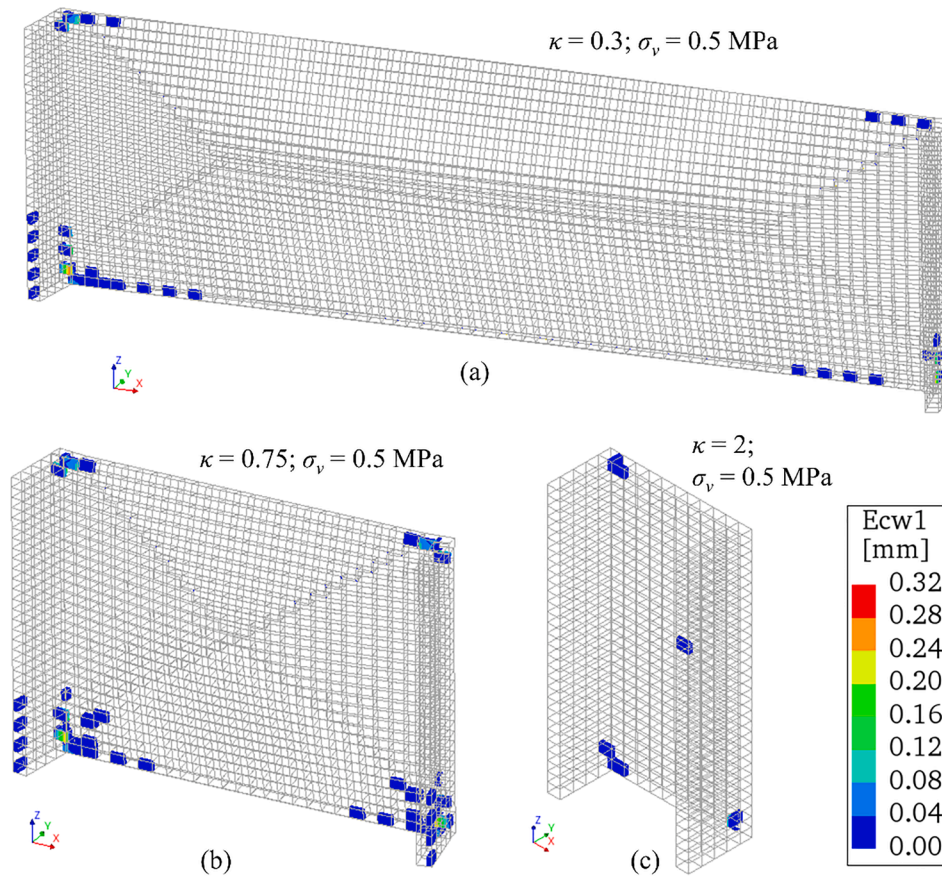


Fig. 14. The tensile failure of the bricks in cases: (a)  $\kappa = 0.3$ ,  $\sigma_v = 0.5$  MPa; (b)  $\kappa = 0.75$ ,  $\sigma_v = 0.5$  MPa; (c)  $\kappa = 2.0$ ,  $\sigma_v = 0.5$  MPa. Ecw1 is the principle crack width.

difference between the fitted function and the numerical results are quite small. The standard error of regression (SER) was introduced to evaluate the average distance that the numerical results deviate from the regression line. A smaller value of SER indicates that the numerical results are closer to the regression line. The SER of Eq. (9) is 0.39 kPa, which means the regression is quite successful. The constants  $a_1$ - $a_5$  represent other crucial factors, such as material properties and boundary conditions, which are non-variables in the equation. It should be noted that till now this equation is more of statistical meaning rather than mechanical meaning. Nevertheless, it perfectly reflects the numerical results. Therefore, Eq. (9) will be compared with current major analytical formulations in the following section to further explore the limitations of the latter.

$$w_{fitted} = a_1 e^{a_2 \kappa} \cdot (a_3 \sigma_v + a_4) + a_5$$

$$\begin{cases} a_1 = 1.6302 \\ a_2 = 0.9724 \\ a_3 = 3.1721 \\ a_4 = 1.9568 \\ a_5 = -1.7759 \end{cases} \quad (9)$$

## 6. Comparison with analytical formulations

In this section, predictions by three state-of-the-art analytical formulations are compared with the results of the parametric study in Section 5. The three analytical formulations are Eurocode 6 [31], Australian Standard for Masonry Structures (AS 3700) [32] and formulations proposed by Willis et al. (2006) [33]. The aim is to further reveal the limitations of these formulations and to find the direction of improving them.

### 6.1. Application of the analytical formulations

The methods of applying the analytical formulations are first introduced. The aspect ratio and pre-compression have the same ranges as those in Section 5. The top and bottom boundaries, and the lateral boundaries of the walls were considered as simply supported and partially clamped, respectively. Since partially clamped boundaries are not included in Eurocode 6, the force capacity of the walls can either be evaluated as hinged or clamped at lateral boundaries, which correspond to support condition E and G in Annex E of Eurocode 6, respectively [31]. Therefore, the results of these two cases were averaged and considered as partially clamped. As for AS3700 and the formulation by Willis et al. (2006), the restraint factor of the lateral boundaries  $R_f$  was assumed to be 0.5 to account for partially clamped lateral boundaries, as suggested by previous studies [15,21,22]. The flexural strength of masonry having the failure plane perpendicular to the bed joints,  $f_{x2}$ , which is required as input for Eurocode 6, is not available from the experimental results [22,29]. Therefore,  $f_{x2}$  was evaluated according to Dutch National Annex to Eurocode 6 [47]. The evaluated value of  $f_{x2}$  is 1.92 MPa. For a detailed discussion regarding the application of the analytical formulations, the readers are referred to [10].

### 6.2. Results and discussions

Fig. 21 shows the comparison of the predictions by the analytical formulations with the numerical results. Results show that: Eurocode 6 tends to overestimate the force capacity in general; AS 3700 tends to overestimate the force capacity when the aspect ratio is over 1; Willis et al. (2006) provides the closest predictions. About the relation between the force capacity and the aspect ratio predicted by the analytical formulations, an extra fitting analysis shows that this relation is

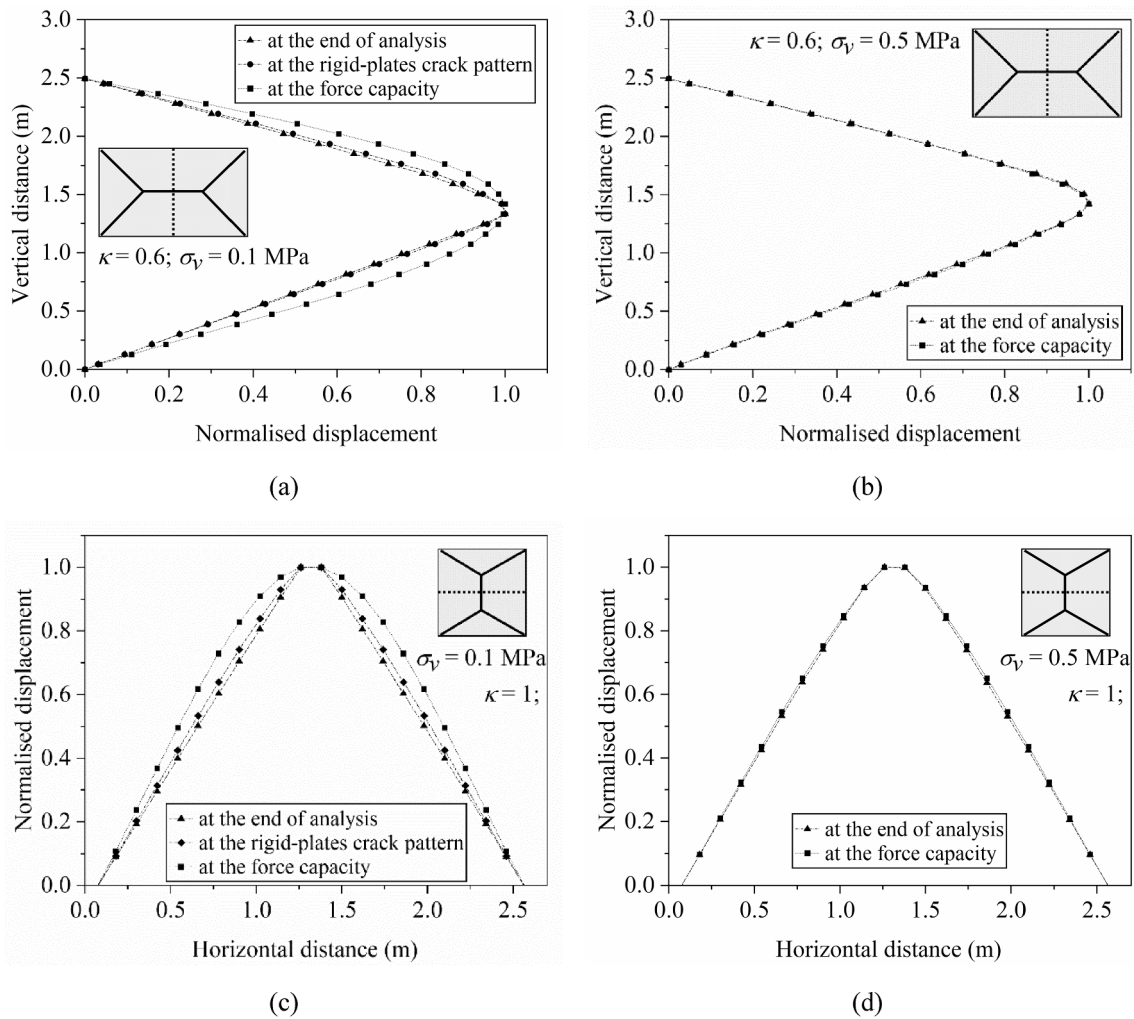


Fig. 15. Deformation profiles of cases: (a)  $\kappa = 0.6$ ,  $\sigma_v = 0.1$  MPa at mid-span; (b)  $\kappa = 0.6$ ,  $\sigma_v = 0.5$  MPa at mid-span; (c)  $\kappa = 1$ ,  $\sigma_v = 0.1$  MPa at mid-height; (d)  $\kappa = 0.6$ ,  $\sigma_v = 0.5$  MPa at mid-height.

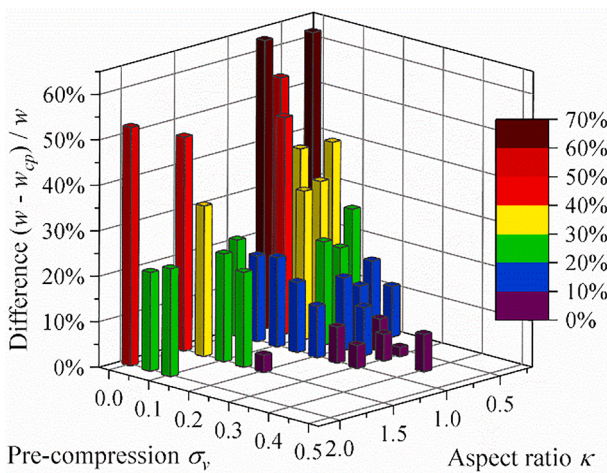


Fig. 16. Differences between the force capacity  $w$  and the force at the final crack pattern  $w_{cp}$  (walls not reaching rigid-plates crack pattern are excluded).

approximately quadratic, which is different from the numerical results reflected in Eq. (9). Concerning the pre-compression, the numerical results show that the force capacity becomes more sensitive to the pre-compression as the aspect ratio increases, while this is not reflected by

the considered analytical formulations. Considering that the contributions to the force capacity by the torsional strength of bed joints are predominant and increase as the pre-compression increases (Section 5.3), also that the evaluation of the torsional capacity of bed joints by the analytical formulations is empirical and insufficient [32,33], it is suggested that more studies should be conducted to determine the relation between the torsional capacity of bed joints and the pre-compression.

More interestingly, the numerical results predict that the influence of the pre-compression and aspect ratio on the force capacity can be interdependent, which is not predicted by any of the three analytical formulations. Equation (9), which precisely fits with the numerical results, indicates that the force capacity is linearly dependent on the pre-compression. As the aspect ratio increases, the slope of the function regarding the pre-compression increases. Consequently, for a wall with a higher aspect ratio, the same increment of pre-compression can have a larger increment of force capacity than that of a wall with a lower aspect ratio. In fact, as observed from Section 5.3, as the pre-compression or aspect ratio increases, the contribution of the torsional capacity of joints increases accordingly. It is therefore rational to deduce that when the aspect ratio increases, the contribution of the torsional capacity of joints increases, and the increase of the pre-compression promotes this effect, thus greatly increasing the force capacity.

The final crack pattern predicted by the Virtual Work method is shown in Table 8. According to the Virtual Work method, if the slope factor  $\alpha$  is larger than 1, a central horizontal crack is predicted;

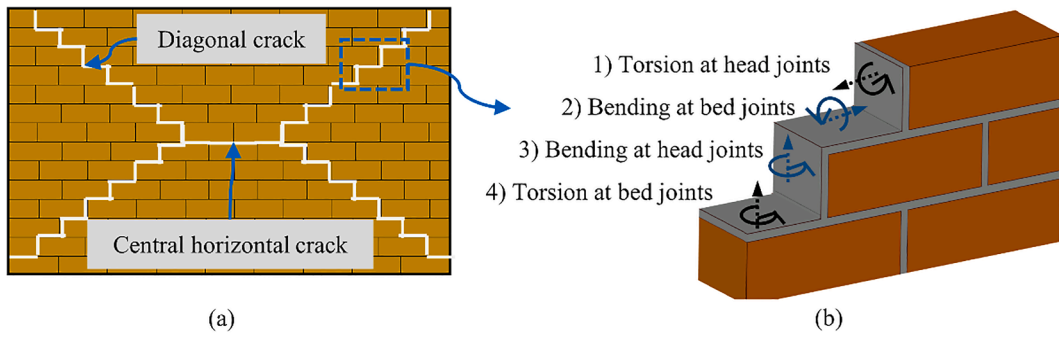


Fig. 17. The calculation for fracture energy dissipated in joints: (a) major cracks along which fracture energy is calculated; (b) joint failure mechanisms.

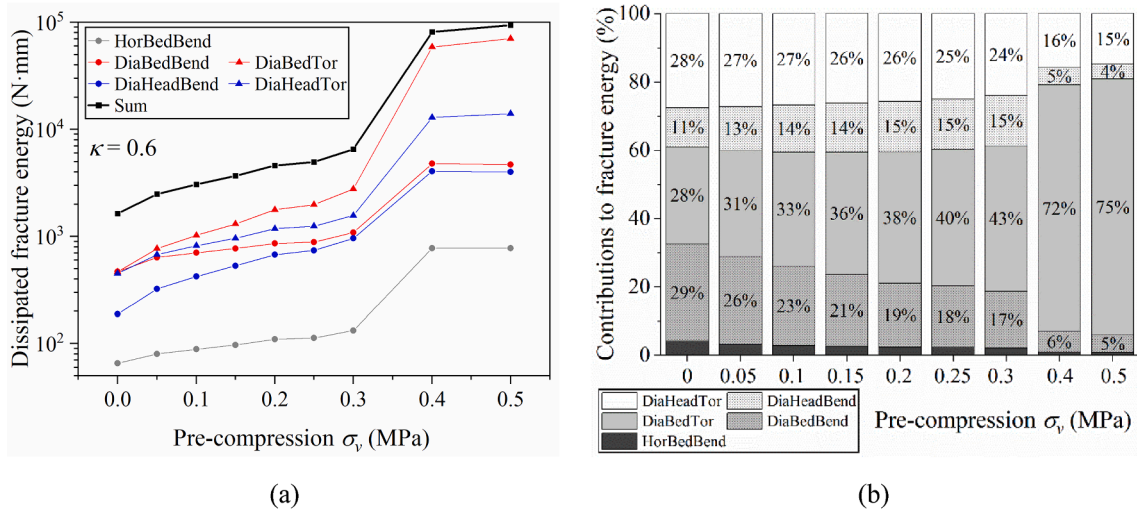


Fig. 18. Influence of the pre-compression on the joint failure mechanisms: (a) dissipated fracture energy by the failure mechanisms; (b) proportions of contributions by the failure mechanisms (abbreviations in the legend: “Dia”: diagonal cracks; “Hor”: central horizontal cracks; “Bed”: bed joints; “Head”: head joints; “Bend”: bending; “Tor”: torsion).

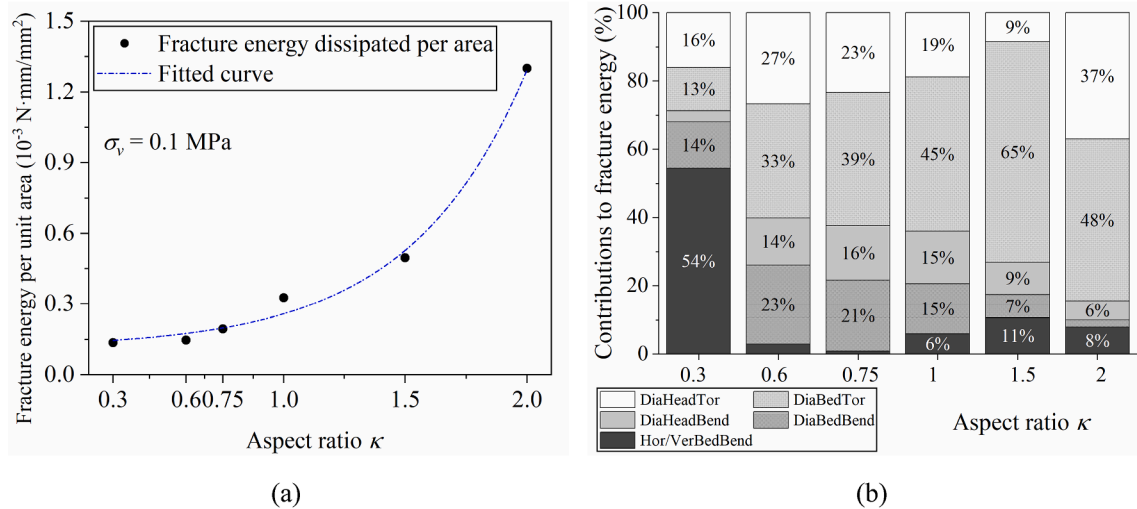


Fig. 19. Influence of the aspect ratio on the crack failure mechanisms: (a) fracture energy dissipated per unit area of walls with various aspect ratio; (b) contributions by the failure mechanisms (abbreviations in the legend: “Dia” – diagonal cracks; “Hor/Ver” – central horizontal or vertical cracks; “Bed”: bed joints; “Head”: head joints; “Bend”: bending; “Tor”: torsion).

otherwise, a central vertical crack is predicted [32]. Results show that when the aspect ratio is smaller than 0.6, central horizontal cracks will appear. Besides, the pre-compression does not influence the crack pattern. These results are in accordance with the numerical results, as

are shown in Table 7. However, it should be noted that according to the numerical results, the walls have not reached rigid-plates crack pattern at the force capacity. The force capacity can be much higher than the force when the wall forms the rigid-plates crack pattern, especially when

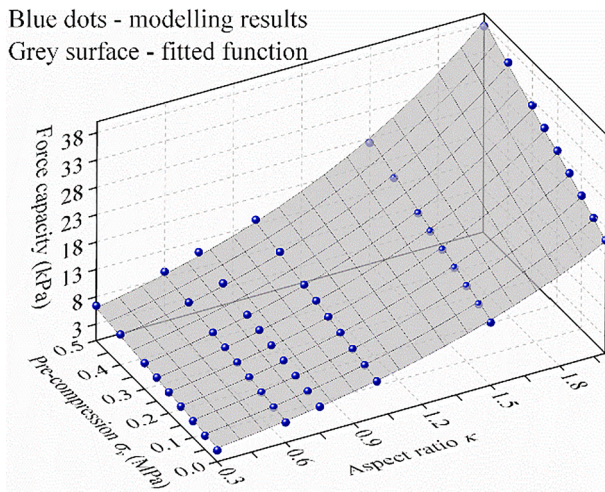


Fig. 20. Numerical results versus fitted function (blue dots: the numerical results; grey surface: the surface of the fitted function). SER = 0.39 kPa.

the pre-compression is low. Besides, the deformation shape of a wall at the force capacity is more close to curved surface rather than rigid plane plates. These observations are against the assumptions of the Virtual Work method. Therefore, the assumption of the deformed shapes of walls at the force capacity is suggested to be re-evaluated.

7. Concluding remarks

This study focuses on the influence of the aspect ratio (wall height to length) and pre-compression on the force capacity of unreinforced masonry (URM) walls in out-of-plane (OOP) two-way bending. The main objectives are i) to quantify the relations between the aspect ratio/pre-compression and the force capacity, and ii) to point out potential directions for improving the accuracy of existing analytical formulations. For these purposes, numerical models were calibrated and validated based on the monotonic quasi-static tests carried out by Griffith and Vaculik [22]. The validated model was further applied in a parametric study in which the aspect ratio (ranging from 0.3 to 2) and pre-compression (ranging from 0 to 0.5 MPa) were double variables. The

influence of the pre-compression and aspect ratio on the force capacity, crack progression, deformation profiles and joint failure mechanisms were studied. Based on the results of the parametric study, a nonlinear fitted equation was proposed to quantify the relations between the aspect ratio/pre-compression and the force capacity. The results of the parametric study were compared with the predictions by three major analytical formulations, namely Eurocode 6 [31], the Australian Standard for Masonry structures (AS 3700) [32] and Willis et al. (2006) [33]. The main findings and conclusions are drawn here.

1. A good agreement is found in terms of the force capacity, initial stiffness and crack pattern between the numerical and experimental results. However, the numerical results show a sharp drop of capacity in the post-peak stage, while the quasi-static experiments provide a more ductile post-peak behaviour. A sensitivity study shows that the low post-peak force in the calibrated model is not sensitive to the material properties and boundary conditions. Nevertheless, the numerically observed post-peak response is in line with other findings in the literature regarding experimental and numerical works [21,42,43]. Therefore, the calibrated model is sufficient to address the purpose of this study.
2. The parametric study shows that the force capacity is exponentially related to the aspect ratio and linearly related to the pre-compression. An interesting finding is that the influence of the aspect ratio and pre-compression on the force capacity can be interdependent. That is, as the aspect ratio increases, the same increment of the pre-compression can lead to a larger increment of the force capacity.
3. The parametric study also shows that the force capacity of walls is much higher than the force at the instant of reaching the rigid-plates crack pattern in the post-peak stage, especially when the pre-compression is low. Also, the deformed shapes of the walls at the force capacity are more close to curved surfaces rather than a group of rigid plane plates. This is against the assumption of the analytical formulations that when the force capacity is reached, the rigid-plates crack pattern has been formed. It is therefore suggested that the deformed shape of the wall at the force capacity (especially when the pre-compression is low) should be studied further.
4. The torsional failure of bed joints is the predominant failure mechanism for URM walls in OOP two-way bending. As the pre-

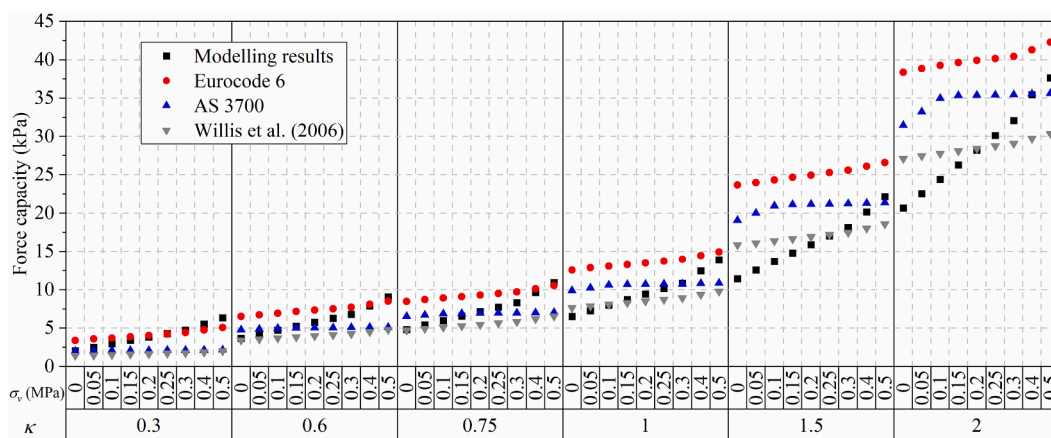


Fig. 21. Comparison of predictions by analytical formulations with numerical results.

Table 8

Final crack patterns predicted by the Virtual Work method.

Aspect ratio $\kappa$	0.3	0.6	0.75	1.0	1.5	2.0
Slope factor $\alpha$	2.39	1.19	0.96	0.72	0.48	0.36
Central crack	Horizontal	Horizontal	Vertical	Vertical	Vertical	Vertical

compression or aspect ratio increases, the proportion of contribution by the torsional capacity of bed joints increases. This suggests that when the aspect ratio increases, the contribution of the torsional behaviour of joints increases, and the increase of the pre-compression enhances this effect thus significantly increasing the force capacity.

- The predictions by the analytical formulations show that: Eurocode 6 tends to overestimate the force capacity in general; AS 3700 tends to overestimate the force capacity when the aspect ratio is over 1; Willis et al. (2006) provides the closest predictions. Besides, the interdependency of the influence of the pre-compression and aspect ratio on the force capacity cannot be predicted by any of the considered analytical formulations.

Based on the aforementioned findings, the following suggestions are proposed aiming at improving the analytical formulations in the standards: the quantitative relations between the force capacity and pre-compression/aspect ratio from the numerical study should be considered; the assumption of rigid-plates cracking pattern forming at the force capacity should be reappraised; the influence of the torsional failure of bed joints on the energy dissipation and force capacity should be studied both experimentally and numerically. At last, it should be clarified that the quantified relationships and proposed equations in this paper are limited to weak joint/strong brick masonry and certain boundary conditions. To further generalise the findings in this study and eventually update the codes for the practical designers, research on different material properties and boundary conditions are recommended.

#### CRedit authorship contribution statement

**Lang-Zi Chang:** Conceptualization, Methodology, Formal analysis, Writing – original draft, Writing – review & editing, Visualization. **Jan G. Rots:** Writing – review & editing, Supervision. **Rita Esposito:** Conceptualization, Methodology, Writing – review & editing, Supervision.

#### Declaration of Competing Interest

The authors declare that they have no known competing financial interests or personal relationships that could have appeared to influence the work reported in this paper.

#### Acknowledgement

The authors would like to express their gratitude to Dr Michael Griffith and Dr Jaroslav Vaculik for sharing the original experimental data. The authors also gratefully acknowledge the anonymous reviewers for their constructive comments and suggestions on the improvement of the manuscript. The financial support provided by the China Scholarship Council (CSC) to the first author is acknowledged. Special thanks from the first author also go to Miss Fortune for her encouragement and company all the time.

#### References

- D'Ayala DF, Paganoni S. Assessment and analysis of damage in L'Aquila historic city centre after 6th April 2009. *Bull Earthq Eng* 2011;9(1):81–104.
- Moon L, Dizhur D, Senaldi I, Derakhshan H, Griffith M, Magenes G, et al. The Demise of the URM Building Stock in Christchurch during the 2010–2011 Canterbury Earthquake Sequence. *Earthq Spectra* 2014;30(1):253–76.
- Penna A, Morandi P, Rota M, Manzini CF, da Porto F, Magenes G. Performance of masonry buildings during the Emilia 2012 earthquake. *Bull Earthq Eng* 2014;12(5):2255–73.
- Sorrentino L, D'Ayala D, de Felice G, Griffith MC, Lagomarsino S, Magenes G. Review of Out-of-Plane Seismic Assessment Techniques Applied To Existing Masonry Buildings. *Int J Archit Herit* 2016:1–20.
- Dizhur D, Ingham J. Seismic Improvement of Loadbearing Unreinforced Masonry Cavity Walls. Report - Branz ER3 New Zealand 2015.
- Walsh KQ, Dizhur DY, Shafei J, Derakhshan H, Ingham JM. In Situ Out-of-Plane Testing of Unreinforced Masonry Cavity Walls in as-Built and Improved Conditions. *Structures* 2015;3:187–99.
- Graziotti F, Tomassetti U, Penna A, Magenes G. Out-of-plane shaking table tests on URM single leaf and cavity walls. *Eng Struct* 2016;125:455–70.
- Doherty K, Griffith MC, Lam N, Wilson J. Displacement-based seismic analysis for out-of-plane bending of unreinforced masonry walls. *Earthquake Eng Struct Dyn* 2002;31(4):833–50.
- Derakhshan H, Griffith MC, Ingham JM. Out-of-Plane Behavior of One-Way Spanning Unreinforced Masonry Walls. *J Eng Mech* 2013;139(4):409–17.
- Chang L-Z, Messali F, Esposito R. Capacity of unreinforced masonry walls in out-of-plane two-way bending: A review of analytical formulations. *Structures* 2020;28:2431–47.
- Chong VL. The behaviour of laterally loaded masonry panels with opening (PhD thesis). Plymouth, UK: University of Plymouth; 1993.
- van der Pluijm R. Out-of-plane bending of masonry behaviour and strength (PhD thesis). Eindhoven, Netherland: Eindhoven University of Technology; 1999.
- van der Pluijm R. 2001-CON-BM-R5015: Laterally Loaded Masonry Panels made with Thin Layer Mortar. Delft, the Netherlands: TNO; 2001.
- Ng CL. Experimental and theoretical investigation of the behaviour of brickwork cladding panel subjected to lateral loading (PhD thesis). Edinburgh, UK: University of Edinburgh; 1996.
- Derakhshan H, Lucas W, Visintin P, Griffith MC. Out-of-plane Strength of Existing Two-way Spanning Solid and Cavity Unreinforced Masonry Walls. *Structures* 2018;13:88–101.
- Griffith MC, Vaculik J, Lam NTK, Wilson J, Lumantarna E. Cyclic testing of unreinforced masonry walls in two-way bending. *Earthquake Eng Struct Dyn* 2007;36(6):801–21.
- Messali F, Ravenshorst G, Esposito R, Rots JG. Large-scale testing program for the seismic characterization of Dutch masonry walls. In Proceedings of the 16th European Conference on Earthquake Engineering, 16WCEE. Santiago, Chile; 2017.
- Damiola M, Esposito R, Messali F, Rots JG. Quasi-static cyclic two-way out-of-plane bending tests and analytical models comparison for URM walls. In 10th International Masonry Conference. Milan, Italy; 2018.
- Padalu PKVR, Singh Y, Das S. Cyclic two-way out-of-plane testing of unreinforced masonry walls retrofitted using composite materials. *Constr Build Mater* 2020;238:117784. <https://doi.org/10.1016/j.conbuildmat.2019.117784>.
- Vaculik J, Griffith MC. Out-of-plane shaketable testing of unreinforced masonry walls in two-way bending. *Bull Earthq Eng* 2018;16(7):2839–76.
- Graziotti F, Tomassetti U, Sharma S, Grotoli L, Magenes G. Experimental response of URM single leaf and cavity walls in out-of-plane two-way bending generated by seismic excitation. *Constr Build Mater* 2019;195:650–70.
- Griffith MC, Vaculik J. Out-of-plane flexural strength of unreinforced clay brick masonry walls. *TMS Journal* 2007;25:53–68.
- Rots JG, van der Pluijm R, Vermeltoot AT, Janssen HJM. *Structural Masonry - An experimental/numerical basis for practical design rules*. Netherlands: A.A. Balkema; 1997.
- D'Altri AM, de Miranda S, Castellazzi G, Sarhosis V. A 3D detailed micro-model for the in-plane and out-of-plane numerical analysis of masonry panels. *Comput Struct* 2018;206:18–30.
- D'Altri AM, Messali F, Rots J, Castellazzi G, de Miranda S. A damaging block-based model for the analysis of the cyclic behaviour of full-scale masonry structures. *Eng Fract Mech* 2019;209:423–48.
- Abdulla KF, Cunningham LS, Gillie M. Simulating masonry wall behaviour using a simplified micro-model approach. *Eng Struct* 2017;151:349–65.
- Haseltine BA, Tutt JN, West HWH. The resistance of brickwork to lateral loading, part II: design of walls to resist lateral loads. *J INST STRUCT ENG* 1977;55:422–30.
- Lawrence S, Marshall R. Virtual work design method for masonry panels under lateral load. In 12th International brick/block masonry conference. Madrid, Spain; 2000, p. 1063–73.
- Vaculik J. Unreinforced masonry walls subjected to out-of-plane seismic actions (PhD thesis). Adelaide, Australia: University of Adelaide; 2012.
- Padalu PKVR, Singh Y, Das S. Analytical modelling of out-of-plane flexural response of unreinforced and strengthened masonry walls. *Eng Struct* 2020;218.
- CEN. Eurocode 6: Design of masonry structures. Part 1-1: General rules for reinforced and unreinforced masonry structures. Brussels, Belgium; 2012.
- Standards Australia International. Australian standard for masonry structures (AS 3700:2018). Sydney, Australia: Standards Australia; 2018.
- Milani Gabriele, Lourenço Paulo, Tralli Antonio. Homogenization Approach for the Limit Analysis of Out-of-Plane Loaded Masonry Walls. *J Struct Eng-Asce* 2006;132(10):1650–63.
- Milani Gabriele, Lourenço Paulo B. Simple Homogenized Model for the Nonlinear Analysis of FRP-Strengthened Masonry Structures. II: Structural Applications. *J Eng Mech* 2013;139(1):77–93.
- Milani Gabriele, Lourenço Paulo B. Simple Homogenized Model for the Nonlinear Analysis of FRP-Strengthened Masonry Structures. I: Theory. *J Eng Mech* 2013;139(1):59–76.

- [41] van der Pluijm R, Rutten H, Ceelen M. Shear Behaviour of Bed Joints. In 12th International Brick/Block Masonry Conference. Madrid, Spain; 2000.
- [42] Karimi Ghaleh Jough Foad, Golhashem Mohammadreza. Assessment of out-of-plane behavior of non-structural masonry walls using FE simulations. Bull Earthq Eng 2020;18(14):6405–27.
- [43] Lawrence SJ. Behavior of brick masonry walls under lateral loading (PhD thesis). Sydney, Australia: University of New South Wales; 1983.
- [44] Li Jie, Masia Mark J, Stewart Mark G. Stochastic spatial modelling of material properties and structural strength of unreinforced masonry in two-way bending. Struct Infrastruct Eng 2017;13(6):683–95.
- [45] Esposito R, Messali F, Ravenshorst GJP, Schipper HR, Rots JG. Seismic assessment of a lab-tested two-storey unreinforced masonry Dutch terraced house. Bull Earthq Eng 2019;17:4601–23.
- [46] Miglietta Marco, Damiani Nicolò, Guerrini Gabriele, Graziotti Francesco. Full-scale shake-table tests on two unreinforced masonry cavity-wall buildings: effect of an innovative timber retrofit. Bull Earthq Eng 2021;19(6):2561–96.
- [47] NEN. NEN-EN 1996-1-1 National Annex to Eurocode 6. Delft, the Netherlands; 2018.